

1 **The overlooked role of westerly moisture as a source of**
2 **summer rainfall in the hyperarid Atacama Desert**

3 **José Vicencio Veloso¹, Christoph Böhm¹, Jan H. Schween¹, Ulrich Löhnert¹,**
4 **and Susanne Crewell¹**

5 ¹Institute of Geophysics and Meteorology (IGM), University of Cologne, Cologne, Germany

6 **Key Points:**

- 7 • Summer moisture transport, named Moist Northerlies (MNs), brings free tropo-
8 sphere humidity from the tropical Pacific to the Atacama
9 • Along with diurnal circulation, MNs lead to 75% of austral summer rainfall days
10 in the Atacama's hyperarid core
11 • MN frequency has been increasing in the last decades, enhancing water vapor and
12 rainfall in the Atacama

Corresponding author: Jose Vicencio Veloso, jvicenc1@uni-koeln.de

13 **Abstract**

14 In the Atacama Desert, one of the driest places on Earth, the persistent absence
 15 of water preserves the record of environmental change, making it an invaluable proxy for
 16 studying the evolution of life on Earth. Due to the scarcity of in-situ measurements and
 17 difficulties in satellite remote sensing, information on precipitation characteristics is lim-
 18 ited even for the present climate. Guided by a case study of extreme precipitation in late
 19 January 2019, we derive a conceptual framework to explain how moisture transport com-
 20 bined with the diurnal circulation produces rainfall. We found a synoptic pattern that
 21 we named "moist northerlies" (MNs) based on surface observations, reanalysis, and high-
 22 resolution simulation. During an MN event, moisture transport from the Tropical Pa-
 23 cific is observed in the lower free-troposphere in the forefront of an 850 hPa low-pressure
 24 offshore Atacama. The diurnal circulation (Rutllant Cell) transports the moist free tro-
 25 pospheric air inland above the coastal marine boundary layer, triggering clouds and storms.
 26 Long-term observations (1960–2020) show that most of the rainy days in the hyperarid
 27 core (75%) are triggered by MNs. A trough over the southeast Pacific and a southward
 28 displaced Bolivian High dynamically drives them, occurring more frequently during the
 29 neutral-cold phase of El Niño-Southern Oscillation (ENSO) and phases 7-8-1 of the Madden-
 30 Julian Oscillation (MJO). A trend analysis (1991–2020) reveals that summer water va-
 31 por along the subtropical west coast of South America has increased rapidly due to the
 32 MNs, enhancing summer rainfall in the Atacama. The implications of climate change
 33 and other variability modes are discussed.

34 **Plain Language Summary**

35 The Atacama Desert, known as one of the driest places on Earth, holds vital in-
 36 formation about how life on our planet has evolved over time because its lack of water
 37 preserves records of environmental changes. However, despite the dryness, rainfall is ob-
 38 served with some recurrence without being completely understood so far. This study fo-
 39 cuses on understanding the mechanisms behind summer rain in the driest part of the At-
 40 acama Desert. We started investigating a specific extreme rainfall event in January 2019,
 41 discovering a weather pattern called "moist northerlies" (MNs) that transport moisture
 42 hundreds and thousands of kilometers from the Tropical Pacific to the desert. The mois-
 43 ture is transported inland during the day, triggering rain in the Atacama. Over several
 44 decades, we found that MNs cause most rainy days in the desert. These MN events seem
 45 to be influenced by larger weather patterns like the El Niño-Southern Oscillation and
 46 the Madden-Julian Oscillation. Additionally, a rapid increase in humidity has been ob-
 47 served along the west coast of South America in recent decades, leading to more sum-
 48 mer rainfall in the Atacama and greening in the Andean precordillera. This study also
 49 discusses how climate change and natural variability might affect the MNs.

50 **1 Introduction**

51 The Atacama Desert, located on the west coast of South America (18–28°S), is well-
 52 known for its extreme hyperaridity. It is characterized by remarkably low rainfall in the
 53 hyperarid core (0.15–5 mm year⁻¹, Fig 1a, Houston & Hartley, 2003), low atmospheric
 54 moisture, and high solar radiation (Rondanelli et al., 2015). The unique desert ecosys-
 55 tem is a natural laboratory for studying the limits of life on Earth and the processes shap-
 56 ing arid environments, which are part of the main objectives of the Collaborative Re-
 57 search Center project 1211 "Earth-Evolution at the dry limit" (CRC1211, Dunai et al.,
 58 2020). Despite being infrequent, rainfall is observed mainly in austral winter linked with
 59 mid-latitude disturbances, e.g., cold fronts (Vuille et al., 1998) and cut-off lows (COLs,
 60 Barrett et al., 2016; Reyers & Shao, 2019). Furthermore, Moisture Conveyor Belts (MCBs)
 61 transport moisture from remote sources, such as the Amazon Basin and the tropical Pa-

62 cific, across the Southeast Pacific towards the Atacama and account for 40-80% of the
63 mean annual precipitation (Böhm et al., 2021).

64 The influence of the above-mentioned mechanisms decreases towards the northeast
65 of the Atacama, resulting in a drier winter season. Consequently, the northeastern part
66 of the desert is dominated by austral summer rainfall (Fig. 1a, e.g., Houston & Hart-
67 ley, 2003; Reyers et al., 2020), for which mechanisms and moisture sources remain de-
68 bated. The hyperarid core, located mainly but not exclusively <2000 m above sea level
69 (ASL), is mostly devoid of long-term observations, making climatological investigations
70 of precipitation challenging. Rainfall increases towards the eastern edge of the Atacama
71 (Precordillera, 2000–3500 m above sea level, ASL) and the Andes plateau (Altiplano, >3500
72 m ASL), with amounts exceeding 50 mm year⁻¹ almost all of which is observed in sum-
73 mer (Vuille et al., 1998; Garreaud, 1999). Here, the occurrence of local storms is induced
74 by moist convection, especially when large-scale conditions strengthen easterly winds over
75 the Andes, i.e., a southward displaced Bolivian High (BH), facilitating the transport of
76 moisture from the interior of the continent (Garreaud & Aceituno, 2001) as part of the
77 South American Monsoon. Some of these storms may propagate westwards from the Al-
78 tiplano, causing rainfall to spill over into the desert (Reyers et al., 2020). However, the
79 Atacama is located leeward of the episodic easterly flow, which typically leads to dry con-
80 ditions by the rainshadow effect described by Houston and Hartley (2003). As a result,
81 the spillover impact seems confined to the easternmost sector of the desert and cannot
82 fully explain the occurrence of rainfall and storms along the hyperarid core.

83 Related to the easterly transport across the Altiplano, the interior continent is fre-
84 quently considered to be the predominant moisture source for summer precipitation (e.g.,
85 Valdivielso et al., 2020). This is relevant because the source region determines the iso-
86 topic composition of water extracted from geological archives (Jordan et al., 2019). How-
87 ever, recent studies suggest the dominance of Pacific-originated moisture as the source
88 of summer rainfall in the Atacama. For an extreme rainfall case study in the summer
89 of 2020, Vicencio (2021) showed that strong moisture transport from the tropical East-
90 ern Pacific at the foreside of a low-pressure system over the Southeast Pacific located
91 in ~ 850 hPa led to widespread storms in the hyperarid core of the Atacama Desert. Us-
92 ing long-term regional climate simulations, Reyers et al. (2020) identified a cluster of rain-
93 fall events in the precordillera triggered by anomalous low-level moist air at the west of
94 the Andes, transported upslope by the so-called Rutllant Cell (Rutllant et al., 2013). Also,
95 Böhm et al. (2021) found a relatively high frequency of nighttime fog in the Precordillera
96 in summer. It seems likely that westerly air-mass uplift along the steep Andes cordillera
97 leads to saturation and cloud formation near the surface. Given the role of the Rutllant
98 cell in transporting air from the coast to the Altiplano during the day as a result of sur-
99 face heating of the Andes, it is highly conceivable that the rain and fog may originate
100 primarily from westerly moisture rather than from an overflow of the Altiplano storms.
101 However, to our knowledge, no study has explicitly discussed this moisture transport mech-
102 anism.

103 The role of large-scale oscillations in influencing summer precipitation has not been
104 fully explored. The Madden-Julian Oscillation (MJO) has been linked to the devastat-
105 ing floods that occurred in central and southern Atacama in March 2015. Strong con-
106 vection over the western Pacific triggered a Rossby wave pattern across the Pacific basin,
107 forming a COL, enhancing moisture transport from the tropics, and triggering intense
108 precipitation (Rondanelli et al., 2019). However, whether the MJO influence on precip-
109 itation is a constant pattern or an exceptional case is not clear. Similarly, the influence
110 of the El Niño-Southern Oscillation (ENSO) on summer rainfall in the Atacama is likely
111 limited to the Altiplano. Here, it has been shown that La Niña weakens the westerly winds
112 in the mid-upper troposphere, increasing the easterly moisture flux and triggering pre-
113 cipitation over this region (Garreaud et al., 2003). The underlying moisture transport

114 mechanisms must be investigated in more detail to study the influence of ENSO and MJO
 115 on summer rainfall in the hyperarid core.

116 Aside from potential large-scale patterns driving precipitation variability, under-
 117 lying trends of ambient atmospheric conditions and synoptic patterns may change the
 118 rainfall regime over time. However, due to the limited availability of long-term obser-
 119 vations, climate change’s impact on summer precipitation is still unclear. Some studies
 120 based on surface weather station measurements have suggested an increase in summer
 121 rainfall in recent decades. E.g., Meseguer-Ruiz et al. (2020) found a positive trend in to-
 122 tal accumulated rainfall for the period 1966–2015 close to Arica ($\sim 18^\circ\text{S}$), as well in the
 123 precordillera and some areas of the Altiplano up valley from Calama ($\sim 23^\circ\text{S}$). For a more
 124 recent period (1990–2019), Olivares (2020) confirms a generalized positive summer trend
 125 for the main stations in the hyperarid core, as well as in the precordillera and western
 126 Altiplano. Heidinger et al. (2018) discovered an increase in very intense rainfall days over
 127 Southern Peru from 1965 to 2010 by studying rainfall indices derived from satellites, in-
 128 dicating an increase in convective activity. These studies emphasize the importance of
 129 investigating long-term changes in moisture supply in the hyperarid core of Atacama and
 130 its potential impacts on precipitation.

131 We hypothesize that austral summer rainfall events in the hyperarid core of the
 132 Atacama are mainly triggered by moisture from the Pacific Ocean. To test this hypoth-
 133 esis, we first analyze an extreme precipitation event that occurred in late January 2019.
 134 We apply reanalysis data aided by regional-scale high-resolution weather simulations,
 135 ground-based remote sensing, and weather stations to mitigate the effects of the com-
 136 plex topography of the Atacama and Andes Cordillera. Second, we perform a climato-
 137 logical analysis (1960–2020) by identifying rainfall days in the hyperarid core from rep-
 138 resentative weather stations. We classify the circulation patterns for each day by their
 139 similarities. We conclude our research by investigating trends in moisture and circula-
 140 tion patterns along the Southeast Pacific that could explain the observed changes in sum-
 141 mer rainfall.

142 2 Data and methods

143 2.1 Rain gauges and remote sensing

144 For the 2019 case study, we use daily accumulated rainfall for the period from 28
 145 to 31 January 2019 for 84 stations in the Atacama ($17\text{--}24^\circ\text{S}$) provided by the Center for
 146 Climate and Resilience Research (CR2: <http://explorador.cr2.cl>). These stations are lo-
 147 cated in the hyperarid core of Atacama (<2000 m ASL), the Precordillera (2000–3500
 148 m ASL), and Altiplano (>3500 m ASL, Fig. 1b). To gain insight into Atacama’s sur-
 149 face circulation, we use specific humidity, wind, and rainfall from a group of four weather
 150 stations available via the Collaborative Research Centre database (CRC1211, Hoffmeis-
 151 ter, 2018). All variables are provided as 10-minute averages, and hourly averages are cal-
 152 culated for our analysis. The weather stations shown in Fig. 1b are labeled as 14 (Salar
 153 de Llamara), 15 (Quebrada de Mani), 22 (Cerro San Antonio), and 25 (Quebrada de Soga).

154 From a one-year field campaign at Iquique Airport (IQQ, 20.54°S , 70.18°W , Fig.
 155 1b) total column water vapor (TCWV) and low-resolution vertically resolved specific hu-
 156 midity and potential temperature are used for the January 2019 case study. These data
 157 are retrieved from measurements by a microwave radiometer (MWR), specifically a 14-
 158 channel Humidity and Temperature Profiler (HATPRO, Rose et al., 2005). It performed
 159 high-frequency measurements (1 s) of brightness temperatures in the microwave range,
 160 from which TCWV and humidity profiles are derived (more details in Schween et al.,
 161 2022). We also derived the Low Troposphere Stability (LTS) as the difference between
 162 the potential temperature at 1.5 km ASL and the surface temperature, measured by HAT-
 163 PRO.

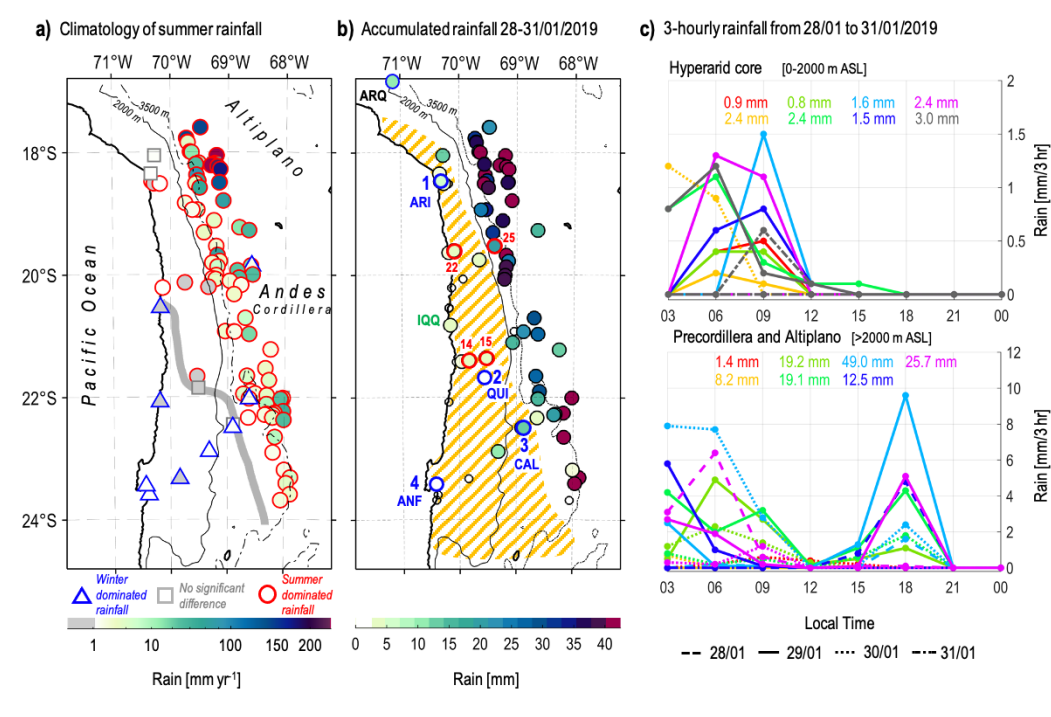


Figure 1. (a) Geographical location of the Atacama Desert and observed mean summer (December–March) rainfall from 1991–2020 for 111 rain-gauges (color-filled circles, in mm yr^{-1}). The gray solid line indicated the approximate border between winter (April–November) dominated rainfall to the south (blue triangles) and summer (December–March) dominated rainfall to the north (red circles). If the difference is not significant (less than 10%), the station is shown as a gray square. (b) Accumulated rainfall from 28–31 January 2019 for 85 rain gauges (color-filled circles, in mm). Red circles denote the four CRC1211 weather stations used for the 2019 case study (stations 14, 15, 22, and 25). Blue circles show the location of the four long-term weather stations: Arica (1 ARI), Quillagua (2 QUI), Calama (3 CAL), and Antofagasta (4 ANF). The location of Arequipa (ARQ) is presented in a black circle. In panels (a) and (b), black lines represent the coastline and terrain altitude at 2000 and 3500 m ASL. The hyperarid core is shown in (b) with a yellow hatch for areas with an annual mean less than 5 mm yr^{-1} . (c) 3-hourly accumulated rainfall between 28 and 31 January 2019 (colored lines) for 15 weather stations in panel (b) with hourly accumulated rainfall available, divided in the hyperarid core (upper panel) and Precordillera and Altiplano (bottom panel) for each day between 28–31 January 2019. The total accumulated rainfall is given in colored numbers at the top panel.

164 For the climatological analysis, we use daily accumulated rainfall from four weather
 165 stations with continuous records from 1960–2020 to identify rainy days in the Atacama’s
 166 hyperarid core and Precordillera. The stations are Arica (1 ARI, 50 m ASL), Quillagua
 167 (2 QUI, 809 m ASL), Calama (3 CAL, 2321 m ASL), and Antofagasta (4 ANF, 112 m
 168 ASL), shown in Fig. 1b. Data were obtained from the Direccion Meteorologica de Chile
 169 (DMC) for stations 1, 3 and 4, for which 6-hourly precipitation is also available but re-
 170 stricted to the period 1964–2020. From the Direccion General de Aguas (DGA), we ob-
 171 tained daily rainfall for station 2. Using the set of four weather stations, we identified
 172 summer (December–March) rainfall days in the Atacama when more than 0 mm is recorded
 173 at least for one station per day. For example, if 2 stations recorded rainfall on the same

174 day, it is considered as 1 rainfall day. In the 60 years, 96 summer rainfall days were de-
 175 tected (~ 1.6 events per summer), and they are listed in Table S1.

176 **2.2 Regional climate model and reanalysis**

177 We apply data from the ERA5 reanalysis (Hersbach et al., 2020) of the European
 178 Centre for Medium-Range Weather Forecasts (ECMWF). The reanalysis has a time res-
 179 olution of 1 hr and horizontal resolution of $0.25 \times 0.25^\circ$ latitude-by-longitude. We use the
 180 data from 1960 to 2020, only for the summer period (December–March). The surface-
 181 level variables are listed as follows: TCWV, sea surface temperature (SST), boundary
 182 layer height (BLH), and sea level pressure (SLP). The pressure level variables (1000–250
 183 hPa) correspond to vertically resolved specific humidity, temperature, horizontal wind,
 184 and geopotential height. We derive the horizontal humidity flux as the specific humid-
 185 ity times the horizontal wind for each pressure level.

186 Considering the rainy days in the Atacama detected from weather stations from
 187 1960–2020, we use ERA5 to composite daily means for each rainy day of the synoptic
 188 conditions for TCWV, 850 and 500 hPa geopotential height and humidity flux, and 500
 189 hPa geopotential height and winds. We then perform a subjective classification, group-
 190 ing the rainfall cases according to similar synoptic features in the lower and upper free
 191 troposphere. An example of one case of rainfall and its classification according to the
 192 synoptic pattern is shown in Figure S1. The characteristics of the 96 identified rainfall
 193 days are available in Supporting Information 1.

194 To complement point observations and the coarse ERA5 resolution, we use the Weather
 195 Research and Forecasting Model (WRF, Skamarock et al., 2008) for a simulation of the
 196 Atacama desert. Via a double one-way nesting, a horizontal resolution of 6 km is achieved
 197 for the output in the inner domain ($17\text{--}27^\circ\text{S}$, $74\text{--}67^\circ\text{W}$) and a temporal resolution of 3
 198 hr. This simulation is an update from a previous long-term WRF simulation performed
 199 by Meyers (2018) driven by ERA-Interim and 10 km resolution. The 6-km WRF sim-
 200 ulation performs well for precipitation in the hyperarid core (e.g., Wennrich et al., 2024),
 201 and provides a more realistic representation of meteorological conditions over the Ata-
 202 cama due to a much better resolution of the complex topography (i.e., Andes Cordillera)
 203 than ERA5. From this simulation, we use specific humidity, horizontal and vertical winds,
 204 specific cloud liquid water content, and precipitation for the January 2019 case study.

205 **2.3 Large-scale oscillations**

206 To investigate the potential impact of ENSO on summer rainfall within the hyper-
 207 arid core, we obtain monthly SST anomalies for the Niño 3.4 and Niño 1+2 regions. Both
 208 indices are based on the Extended Reconstructed Sea Surface Temperature version 5 (ERSSTv5,
 209 Huang et al., 2017), available from 1950 to nowadays, and obtained from the NOAA’s
 210 Climate Prediction Center database (<https://www.cpc.ncep.noaa.gov/data/indices/>).
 211 Due to the SST warming in the Pacific Basin (L’Heureux et al., 2013), the Niño 3.4 in-
 212 dex has been detrended by NOAA using centered 30-year base periods, moving every five
 213 years. The Niño 3.4 and 1+2 index correspond to the average SST anomalies of the Cen-
 214 tral Pacific ($5^\circ\text{N}\text{--}5^\circ\text{S}$, $170\text{--}120^\circ\text{W}$) and the Eastern Tropical Pacific ($0\text{--}10^\circ\text{S}$, $90\text{--}80^\circ\text{W}$).

215 For the MJO, we use the real-time Multivariate Index for tropical Intraseasonal os-
 216 cillations (rMII, Wang et al., 2022). This index defines the intensity of the MJO as the
 217 leading Empirical Orthogonal Functions (EOF, rMII 1 and rMII 2) of the projection of
 218 9-day running average anomalies of the eastward filtered Outgoing Longwave Radiation
 219 (OLR), and zonal winds at 850 hPa and 200 hPa. The index is available from 1979 to
 220 nowadays and is obtained from the NOAA Physical Science Laboratory (<https://www.psl.noaa.gov/mjo/mjoindex/>). The location of the anomalous convective area that
 221 circles the Planet eastward (Madden & Julian, 1972) is classified into phases labeled from
 222

223 1 to 8, corresponding to the Western Pacific (phases 6–7), America and Africa (phases
224 8–1), Indian Ocean (phases 2–3) and Maritime Continent (phases 4–5).

225 3 Results and discussions

226 3.1 Extreme rainfall case of 2019

227 In the course of an extreme event between 28–31 January 2019, up to 20 mm of
228 rainfall accumulated in some regions of the hyperarid core of the Atacama Desert (<2000
229 m ASL, Fig. 1b), mainly between 0–12 Local Time (LT, Fig. 1c). These amounts are
230 considered extreme compared to the summer mean long-term precipitation. For exam-
231 ple, the stations around Arica recorded up to 3 mm, exceeding ~ 6 times the long-term
232 summer average for this location. The stations with the highest accumulated rainfall in
233 the hyperarid core reached 15–20 mm (Tacna and Sierra Gorda), exceeding 5–10 times
234 the long-term average. On the eastern margin of the Atacama (Precordillera, 2000–3500
235 m ASL) as well as in the Altiplano (>3500 m ASL), rainfall accumulated up to 50 mm
236 (Fig. 1b) with daily peaks around 18 LT and between 00–09 LT (Fig. 1c). This event
237 shows significant rainfall spatial variability across the region, with the lowest values near
238 the coast and increasing to higher lands (Fig. 1b).

239 We investigate the environmental conditions for Iquique (20.5°S) from ground-based
240 measurements (HATPRO) and ERA5. Both time series show a good agreement in mag-
241 nitude and variability during the second half of January (Fig. 2a), consistent with the
242 validation performed between March 2019–March 2020 by Vicencio Veloso et al. (2024).
243 In particular, the increase at the end of January of the ERA5 TCWV agrees with the
244 HATPRO retrievals (from 30 to 55 kg m^{-2}), exceeding the 90th percentile of the reanal-
245 ysis climatology. Moisture increases over most of the troposphere, but the lower free tropo-
246 sphere (900–800 hPa) shows the strongest signal (Fig. S2). At 850 hPa, the specific
247 humidity increased from 3–6 g kg^{-1} before the rain event to almost 12 g kg^{-1} during the
248 event (Fig. 2a). These values are also extreme when compared to the climatology.

249 The synoptic pattern responsible for the extreme coastal TCWV values is charac-
250 terized by a southward displaced Bolivian High (BH) positioned east of the Atacama (23°S,
251 77°W) and a trough over the Southeast Pacific (Fig. 2b). A field of strong poleward-directed
252 winds forms between these upper-level systems, resulting in divergence at its left entrance.
253 This, in turn, supported cyclogenesis in the lower free troposphere starting on 26 Jan-
254 uary, resulting in a cyclonic circulation in 850 hPa offshore the Atacama Desert and en-
255 hanced moisture transport along the west coast of South America from the Tropical Pa-
256 cific in the lower free troposphere (Fig. 2b, Fig. S3).

257 After arriving offshore the Atacama coast, the moisture-enriched free-tropospheric
258 air is transported inland and upslope due to the diurnal circulation induced by the sur-
259 face warming of the west slope of the Andes via the Rutllant Cell. Both stations and WRF
260 show a strong diurnal cycle in the zonal moisture flux, peaking in the afternoon (~ 18
261 LT) and decreasing with elevation more inland (Fig. S4). During the rainfall episode,
262 specific humidity increases from 6 to 12 g kg^{-1} at the lowermost stations and from 5 to
263 10 g kg^{-1} in precordillera. These values are similar to the specific humidity observed at
264 850 hPa offshore Iquique. Additionally, lower troposphere stability (LTS) weakens off-
265 shore Atacama (Fig. 2c), which could allow a more efficient mixing between the MBL
266 and the free troposphere and further increase the transport of coastal moisture towards
267 the interior of the desert that is usually blocked by the strong inversion at ~ 1 km ASL.
268 As a result, the Atacama Desert experiences increasing moisture near the surface, which
269 is decisive to cloud formation and rain.

270 To further understand how moisture transport interacts with local circulation and
271 topography, we focus on the 72 hours between 28 January 12 LT and 31 January 12 LT
272 with surface weather stations (Fig. S4), satellite (Fig. S5), and high-resolution WRF sim-

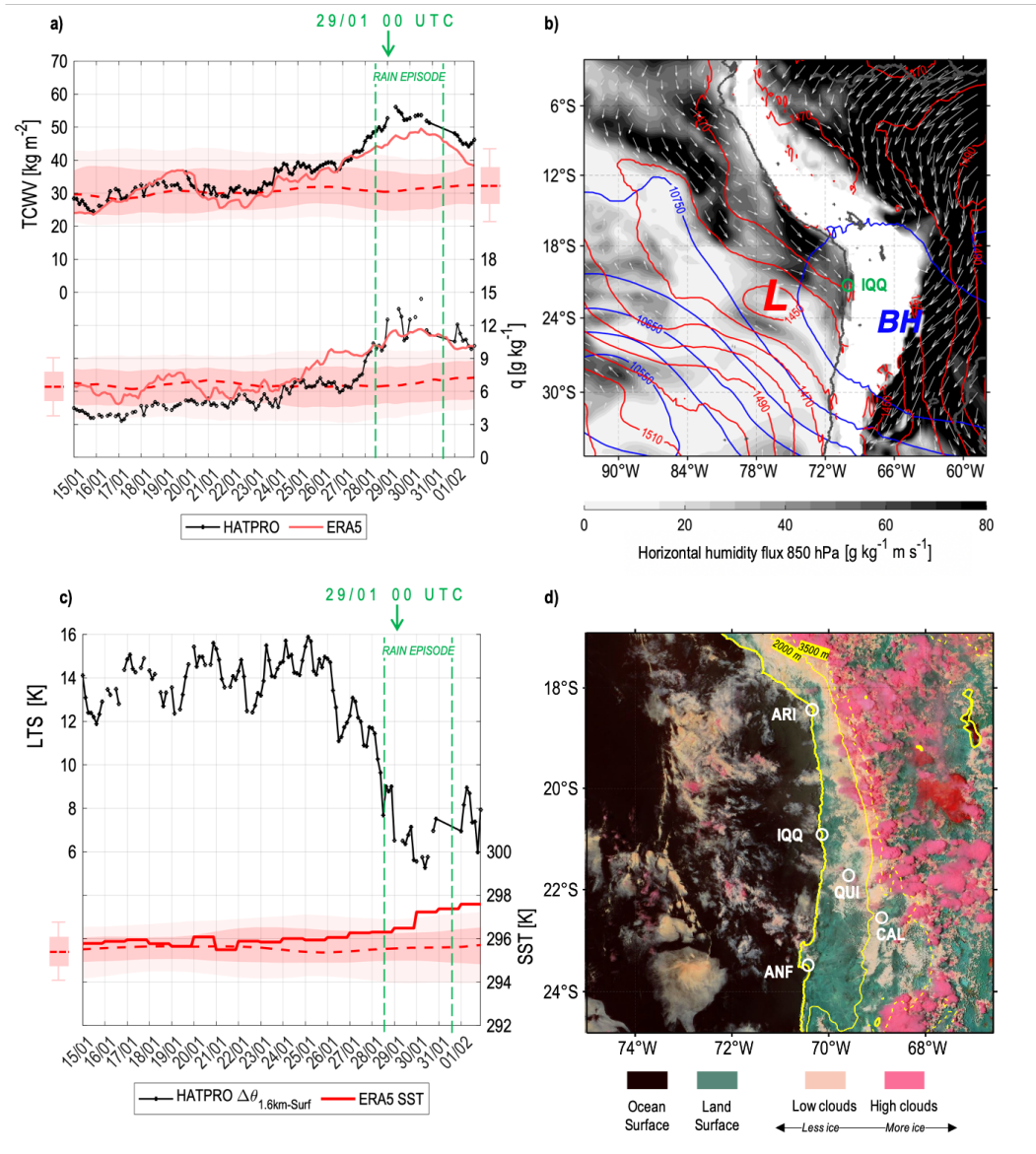


Figure 2. Three-hourly time series of (a) TCWV and specific humidity in 850 hPa, and (c) low troposphere stability (LTS, potential temperature difference between 1.6 km ASL and surface) and SST. Data are shown for HATPRO retrievals (black dotted line) from Iquique Airport (see IQQ location in panel b) and for ERA5 for the average of the four nearest grid points to Iquique (red line). For the SST, the four closest ocean grid points from ERA5 were used. ERA5 climatological (1991–2020) information is provided as a boxplot for the interquartile range, and the upper/bottom whiskers are the 10th/90th percentile, respectively, smoothed with a 30-day window average. (b) 850 hPa humidity flux (shaded color and white arrows above $30 \text{ g kg}^{-1} \text{ m s}^{-1}$), 850 hPa geopotential height (red lines, every 10 m) and 250 hPa geopotential height (blue lines, every 50 m) on 29 January 2019 00 UTC from ERA5. The location of the Bolivian high (BH) and 850 hPa low pressure (L) are indicated. The Andes cordillera is patched white for altitudes above 850 hPa. (d) Cloud snow-ice product (Bands M3-I3-M11) from NOAA-20/VIIRS at 19:03 UTC (15:03 LT) 29 January 2019 (<https://worldview.earthdata.nasa.gov>). Yellow lines represent the coastline and terrain altitude at 2000 and 3500 m ASL. The main weather stations used are also shown in white circles.

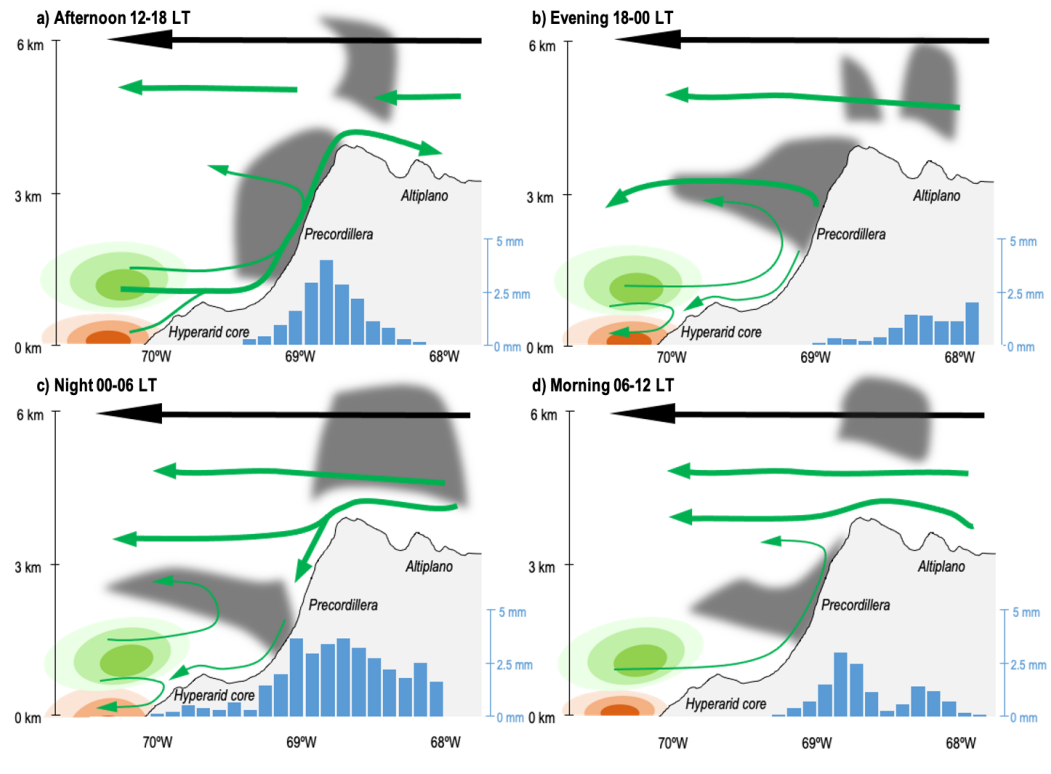


Figure 3. Schematic figure of a cross-section over the Atacama Desert between 18–22°S and 71–68°W for the 2019 extreme rainfall event. Meridional moisture transport from the north and south is shown in green and orange ovals, respectively. Zonal humidity flux is presented in green arrows. In black, the predominant easterly upper troposphere wind is given. Clouds are shown in gray. Rainfall is presented in blue bars ($\text{mm } 6 \text{ hr}^{-1}$). Four-time segments: (a) afternoon (12–18 LT), (b) evening (18–00 LT), (c) night (00–06 LT), and morning (06–12 LT).

273
 274
 275
 276
 277
 278
 279
 280
 281
 282
 283
 284
 285
 286
 287
 288
 289
 290
 291

ulation (Fig. S6). We summarize our findings in the schematic Figure 3. In the afternoon (12–18 LT, Fig. 3a), the Andean pumping peaks in westerly moisture transport from the lower free troposphere offshore Atacama towards the Andes. The forced topographic uplift leads to cloud formation along the hyperarid core, identified as low clouds (mainly stratus clouds). In the Precordillera, the stratiform cloud is also observed but with some cumulonimbus embedded (Fig. 2d, Fig. S5), explaining the enhanced rainfall peak at around 18 LT observed at the weather stations (Fig. 1c). Westerly moisture reaches the Altiplano as far east as 68°W, triggering storms in this region as well (Fig. 3a).

In the evening (18–00 LT, Fig. 3b), the return circulation at 3 km ASL is now coupled with the mid-upper tropospheric easterlies, further inducing cloud development closer to the coast. Easterly winds intensify at night (00–06 LT, Fig. 3c), and the lower tropospheric circulation over the Atacama weakens. Nevertheless, stratiform clouds continue to form over the desert and are displaced towards the west, producing the strongest period of precipitation in the hyperarid core, according to the measurements. Additionally, a descending branch of moisture is observed across the precordillera, potentially inducing rain spillover from Altiplano storms. This pattern is present until the next morning (06–12 LT, Fig. 3d) when the radiative heating of the surface again initiates the westerly moisture flux from the Pacific to the Andes, further inducing cloud formation in the Precordillera.

Our results strongly suggest that this rainfall episode is triggered by moisture coming from the Pacific Ocean transported by moist northerlies in the lower free troposphere, as opposed to the more common Amazonian source connected with easterly winds in the mid-upper troposphere. Further evidence supporting this conclusion can be found in Welp et al. (2022), who measured stable water isotopes at Arequipa (16.3°N, 71.5°W, at 2300 m ASL, Fig. 1b). They found isotopically depleted rain during the period from 31 January 2019 to 14 February 2019 (i.e., the same rainfall event of our study), indicating a predominance of oceanic originated precipitation rather than a continental source. We suspect that these results are also valid for the Atacama, which, although located about 200 km south of Arequipa, is affected by the same low-level synoptic pattern. Furthermore, we found evidence that the Rutllant Cell can transport high humidity levels toward the Atacama when the free-troposphere offshore is moist. This complements the findings of Schween et al. (2020), who described a net moisture transport to the east during daytime between 2017-2019 derived from the CRC1211 weather stations network.

3.2 Composite analysis and teleconnections

Given the strong impact of the case analyzed in Section 3.1, we now want to understand how frequently such cases occur and what their driving mechanisms are. We use the 96 rainfall days identified in the hyperarid core identified from 1960–2020 (see Section 2.1) and group them by similar synoptic characteristics. Most of the rainy days (72 cases, ~75%) have in common a well-developed Bolivian high to the east of the Atacama and an offshore low-pressure at 850 hPa, which induces moisture transport from the north along the southeast Pacific, consistent with the 2019 study case. Based on the strong moisture transport, we refer to these cases as Moist Northerlies (MNs). Another group of rainy days is characterized by a southward displaced BH but without the low-pressure offshore Atacama in the lower free troposphere. Here, rainfall over the Altiplano is likely spilled over the Andean mountain range (9 cases, ~9%). The rest of the rainy days (15 cases, ~15%) show a mid-upper tropospheric trough (TT) or a cut-off low (COL) approaching from the west, inducing large-scale instability and moisture transport to the Atacama.

The number of rainfall days and summer accumulated precipitation associated with each mechanism show large interannual variability (Fig. 4a,b). The MN episodes have a higher recurrence between 1987-1991, 2000-2006, and 2018-2020. In fact, the summer of 2020 shows the highest number of days with precipitation so far (10 days), all associated with MNs. The increase in MN rainfall days is mainly driven by Arica, which observes a significant growth in the number of days and rainfall associated with MNs in the decade 2011-2020 compared to the 60s and 70s (Fig. 4c,d). Summer rainfall in Quilagua has only been observed recently, for which MNs account for 6 rainfall days between 2001–2020. In Calama, the MNs peaked in the decades of 1971–1980 and 2001–2020, with 8 episodes per summer, each accounting for between 16–20 mm. In the southern part of the study area, Antofagasta, MNs peaked in duration and intensity in the 1970s (3 days and ~7 mm), but have not been observed since (Fig. 4c,d).

While the MNs account for 65% of the total rainfall, they are not associated with the most extreme precipitation cases (such as the COLs in 2015, Fig. 4b,d), but they are more recurrent from year to year, becoming the most reliable water source in the hyperarid core. The sub-daily distribution of rainfall intensity for Arica, Antofagasta, and Calama (stations with sub-daily rainfall available) also shows that the MNs are usually associated with light rain (<3.0 mm in 6 hr, Fig. 4e), and often occur during the night (Fig. 4f) in agreement with the 2019 case study. The COL, despite being responsible only for 11% of the rainy days (Fig. 4a), accounts for 25% of the precipitation (Fig. 4b) and higher sub-daily intensity (Fig. 4e).

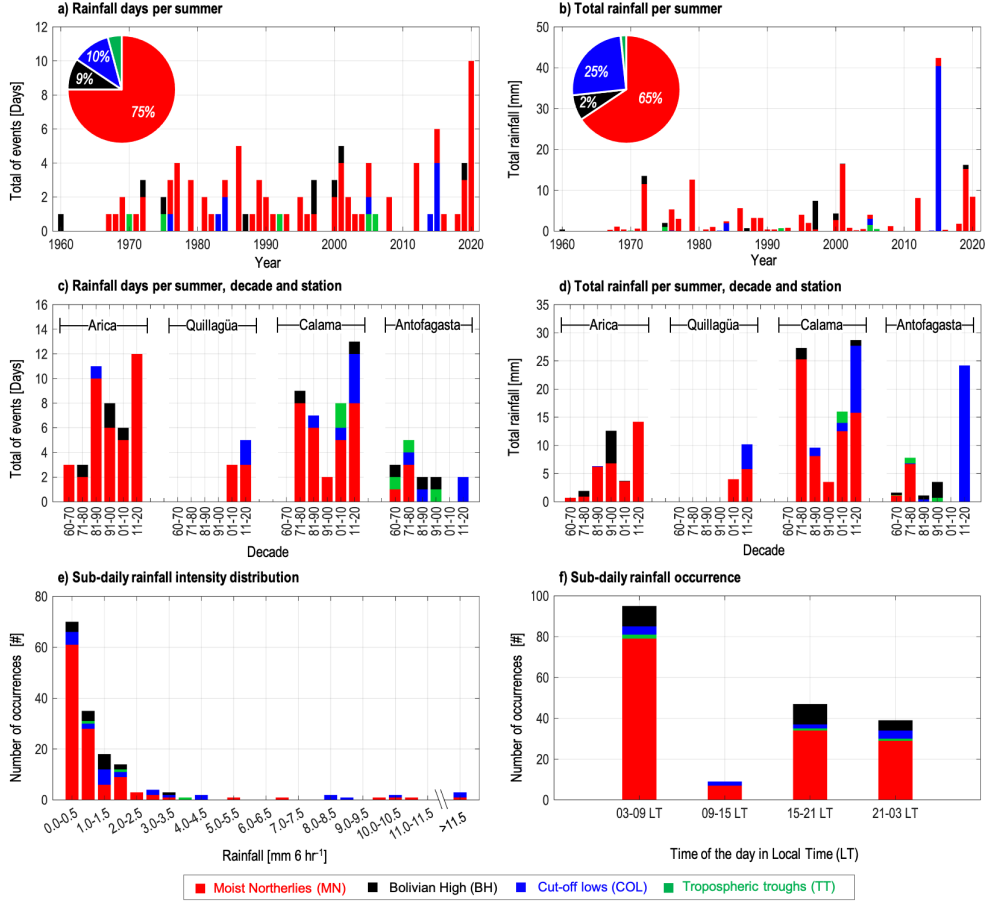


Figure 4. Top: time series of the (a) number of rainy days per summer and (b) total precipitation between 1960–2020, identified from the four weather stations with long-term observations. Middle: decadal (a) rainfall days per summer and (b) total rainfall per summer, divided in the four weather stations used (Arica, Iquique, Calama, and Antofagasta). Bottom: sub-daily distribution of (e) rainfall intensity ($\text{mm } 6 \text{ hr}^{-1}$) and (f) period of rainfall occurrence. The calculation was made for standard periods of 6 hours (i.e., 03–09 LT, 09–15 LT, 15–21 LT and 21–03 LT). This subdaily rainfall data is only available for Arica, Calama, and Antofagasta weather stations for the period 1964–2020. The type of synoptic configuration is identified by colored bars: red for Moist Northerlies (MN), black for the Bolivian High (BH), green for Cut-off Lows (COL), and blue for Tropospheric Troughs (TT).

342 The spatial variability of the rainfall associated with MNs reveals that they rarely
 343 affect the city of Antofagasta, in which only 29% of the precipitation days have been caused
 344 by this mechanism (4 days out of 14). The proportion of rainfall explained by the MNs
 345 increases toward the north and east, reaching 74% in Calama (29 days out of 39), 75%
 346 in Quillagua (6 days out of 8), and 88% in Arica (38 days out of 43). We suspect that
 347 a short distance between the coast and the Andes is crucial to allow the nighttime clouds
 348 and precipitation to reach the shoreline. While in Antofagasta, this distance is $\sim 200 \text{ km}$,
 349 in Arica is roughly 60 km . However, a lack of more weather stations prevents further anal-
 350 yses. To link these rainfall characteristics to the typical synoptic conditions, we inves-
 351 tigate the composite means and anomalies of the atmospheric state for the identified MN
 352 cases in the following.

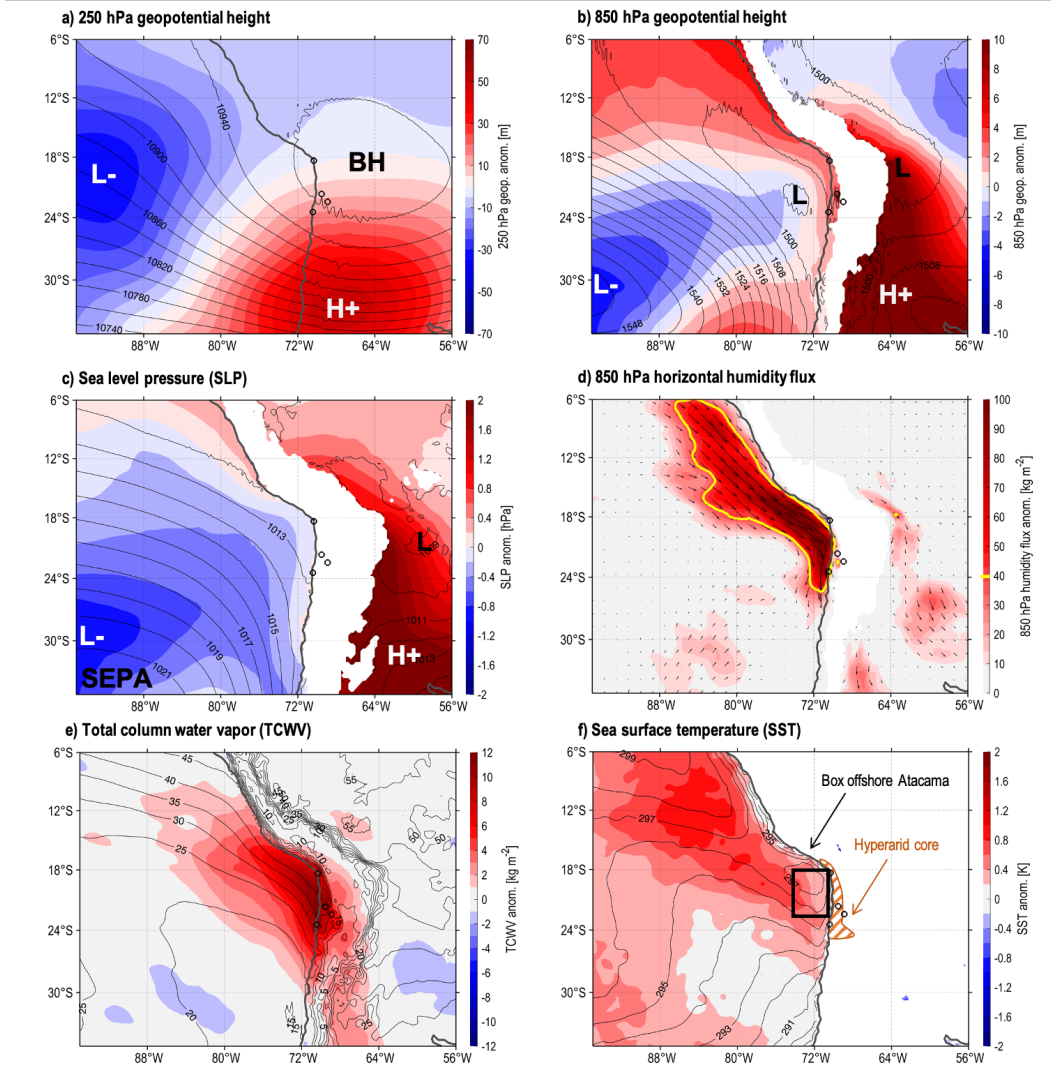


Figure 5. Composite of MN rainfall days ($N = 72$) of the mean of the MN days (black contours) and the mean anomaly of MN days (shaded colors). The anomalies were computed as the difference between each rainfall day and its respective climatological average (1991–2020) for that specific day for: (a) the 250 hPa geopotential height (in m), (b) 850 hPa geopotential height (in m), (c) Sea level pressure (SLP, in hPa), (d) 850 hPa humidity flux (in $\text{g kg}^{-1} \text{m s}^{-1}$), (e) TCWV (in kg m^{-2}), and (f) SST (in K). Low and high-pressure locations are shown in black for the mean and white for anomalies, including the SEPA and BH. Black circles show the location of the four main weather stations for identifying rain events. In panels b, c, and d, the Andes cordillera is patched white for altitudes above 850 hPa. In panel e), the hyperarid core is shown in the orange patch, and the Atacama offshore region ($18\text{--}23^\circ\text{S}$, $74\text{--}71^\circ\text{W}$) is shown in the black box.

353 The MNs composite, derived from ERA5, shows a southward displaced BH, expressed
 354 through a strong 250 hPa ridge anomaly over the central Andes (33°S, 69°W, Fig. 5a).
 355 Concurrently, a trough anomaly is formed to the west of the BH over the southeastern
 356 Pacific (18°S, 95°W). The upper-troposphere anomaly dipole is likely conducive to in-
 357 fluencing the lower levels of the troposphere and forming the 850 hPa low-pressure off-
 358 shore Atacama and a retreat to the south of the Southeast Pacific Anticyclone (SEPA,
 359 Fig. 5b). The low pressure is not projected at the surface, and the SEPA dominates the
 360 composite. Nevertheless, we observe a generalized weakening of the anticyclone over the
 361 Southeast Pacific (Fig. 5c). The weakened SEPA and the 850 hPa low pressure during
 362 MN episodes produce weaker moisture transport from the south within the MBL and
 363 stronger than normal moisture transport from the north in most of the free troposphere,
 364 especially between 900–700 hPa in a box offshore Atacama (18–23°S, 74–70°W, Fig. 6).

365 Similar moisture transport structures in the free troposphere have been described
 366 by Böhm et al. (2021), who used the term MCB. The MCBs detection algorithm is based
 367 on the Guan and Waliser (2015) Atmospheric River (AR) catalog, for which ARs are iden-
 368 tified according to a percentile threshold regarding integrated water vapor transport (IVT)
 369 together with shape criteria. This identification might not be sensitive to the MN dis-
 370 cussed here, for which enhanced northerly moisture transport is limited to the lower free
 371 troposphere over a depth of ~ 200 hPa (Fig. 6). This moisture transport is insufficient
 372 to produce an outstanding IVT signal, given that moist southerlies in the MBL are still
 373 present during the MN episodes, counteracting the integrated moisture transport. This
 374 explains why, from the 15 summer MCBs found by Böhm et al. (2021) between 1979–
 375 2019, none correspond to MN episodes identified in this study. Nevertheless, the hori-
 376 zontal moisture transport structure of the MNs resembles an AR in the lower free tro-
 377 posphere (~ 850 hPa, Fig. 5d), bringing enough humidity to produce above-normal TCWV
 378 anomalies offshore Atacama (Fig. 5e).

379 Warmer than normal SST has been acknowledged as a significant factor in precip-
 380 itation events in the Atacama, primarily by enhancing humidity and instability (Bozkurt
 381 et al., 2016). During MN episodes, SST increases in the Southeast Pacific, with anoma-
 382 lies up to +1 K (Fig. 5f). However, we suspect that this warming is the consequence of
 383 the MN synoptic pattern expressed with the overall weakening of the SEPA (Fig. 5c)
 384 and reduced southerly winds at the surface, which lower the transport of cold waters from
 385 the south and hinder coastal upwelling. Additionally, warmer SST during MN episodes
 386 is typically confined to the coastal areas and coincides with neutral ($\sim 35\%$) or weak La
 387 Niña conditions ($\sim 38\%$) in the Central Pacific (Fig. 7a), and with mainly neutral con-
 388 ditions in El Niño 1+2 ($\sim 69\%$, Fig. 7a). Thus, it is suspected that the observed warm-
 389 ing offshore Perú and northern Chile during MN episodes is predominantly influenced
 390 by changes in atmospheric circulation rather than being the primary cause of the MN
 391 pattern and the associated precipitation.

392 Furthermore, the relationship between La Niña in the Central Pacific and MNs can
 393 be partially explained by the weakening of the subtropical jet due to the reduction of
 394 the meridional temperature gradient between the tropics and mid-latitudes. A weaker
 395 jet stream allows the anomalous southward displacement of the BH (Garreaud et al., 2003),
 396 enhancing the formation of the 850 hPa low-pressure offshore the Atacama and weak-
 397 ening the SEPA. A similar impact can result from the active phases of MJO. For the pe-
 398 riod 1979–2020 (period of data availability of the index), most of the MN cases are re-
 399 lated to phases 7, 8, and 1 ($\sim 40\%$, Fig. 7b). These phases are associated with summer
 400 heatwaves in central Chile (32–38°S, Jacques-Coper et al., 2021; Demortier et al., 2021)
 401 due to a synoptic configuration over the Pacific and South America analogous to the MN
 402 composite, i.e., an exacerbated strong ridge anomaly over the central Andes accompa-
 403 nished by a trough anomaly over the Southeast Pacific. This upper-troposphere pattern
 404 can also contribute to displacing the BH and the SEPA poleward, further helping to form
 405 the 850 hPa low-pressure offshore Atacama. An example of this compound event was

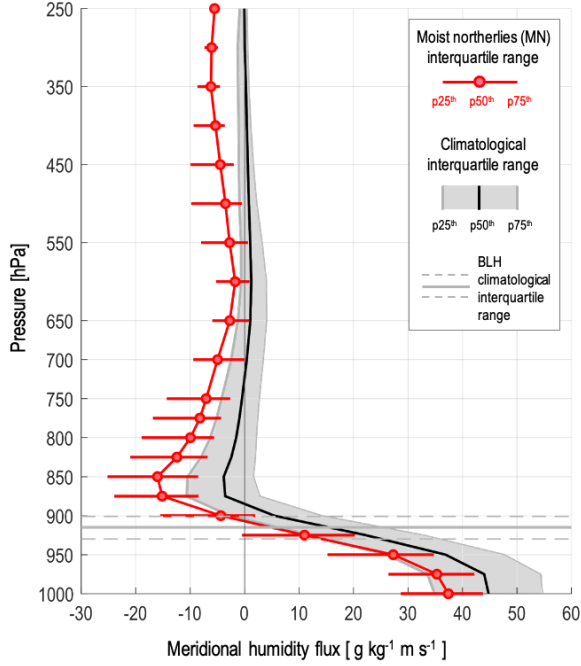


Figure 6. Vertical profile of the meridional humidity flux (red dotted line) for a box offshore Atacama (18-23°S, 74-71°W). The interquartile range for the 72 MN episodes is shown in a red horizontal line, and the summer climatology for the 1991-2020 period is in the gray-shaded polygon. The boundary layer height (BLH) interquartile range climatology is shown in the gray horizontal lines. Data from ERA5.

406 observed during the January 2019 study case, in which several cities south of 33°S recorded
 407 record heat a few days before the extreme rainfall event in the Atacama (Jacques-Coper
 408 et al., 2021). Yet, around 37% of the MN days still occur in the inactive phase of the MJO
 409 (Fig. 7b).

410 3.3 Long-term trends and impacts of MNs

411 Given the importance of MNs in supplying moisture to the Atacama, the question
 412 arises whether their frequency is affected by global climate change. The summer-averaged
 413 TCWV for a box offshore Atacama (18-23°S, 74-71°W) shows a positive trend, especially
 414 evident in the periods starting between 1970-1998 and ending between 2018-2020, rang-
 415 ing from 0.7 to 1.6 kg m⁻² decade⁻¹ (Fig. 8a). These changes in the summer mean are
 416 also observed in the daily means of TCWV (Fig. 8c). The probability distribution shows
 417 that the upper-right tail extends to higher values during the 2011-2020 period compared
 418 to previous decades, with the maximum values shifting from 45 to 55 kg m⁻². The change
 419 in the distribution also includes a shift from an unimodal to a bimodal distribution in
 420 TCWV, e.g., a secondary mode around 40 kg m⁻² appears in the 2011-2020 distribu-
 421 tion (Fig. 8c).

422 The increase in TCWV observed in the box offshore Atacama is part of a regional
 423 pattern in the Southeast Pacific. Taking the period 1991-2020, the mean TCWV trend
 424 reaches up to 2 kg m⁻² decade⁻¹ and is significant at the 95% confidence level offshore
 425 Peru and northern Chile (Fig. 9a). The 90th percentile of summer TCWV shows a sim-

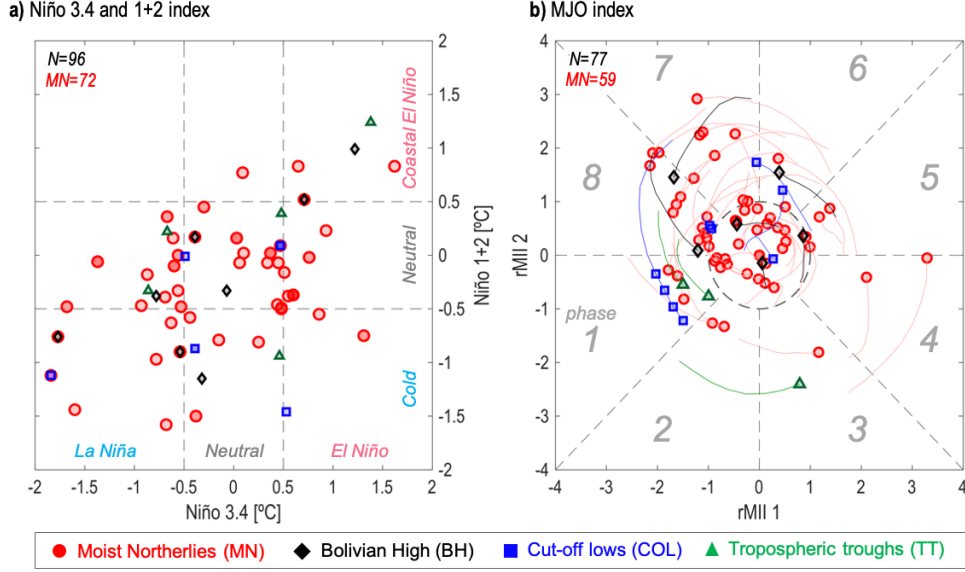


Figure 7. (a) Scatter plot of monthly SST anomalies for Niño 3.4 (x-axis) and Niño 1+2 (y-axis) for each summer rainfall day in the Atacama Desert between 1960–2020, and (b) MJO index (Wang et al., 2022) for each summer rainfall day in the Atacama Desert between 1979–2020. It includes the previous 7-day MJO phase (thin line). In both panels, the color and shape of the symbol represent the type of rainfall mechanism identified: red circle for moist northerlies (MN), black diamonds for the Bolivian High (BH), green triangles for cut-off lows (COL), and blue squares for tropospheric troughs (TT). In the upper left corner, the number of rainy days (N) and the number of rainy days associated with MN are shown.

426 ilar spatial pattern, but almost doubles the trend of the mean, reaching up to 3 kg m^{-2}
 427 decade^{-1} near the Atacama coast (Fig. 9b).

428 The positive TCWV trend results from a general increase in moisture throughout
 429 most of the free troposphere and is most prominent in its lower levels (800-900 hPa, Fig.
 430 10a). We attribute this trend to the rising frequency of the MN condition, this is, a de-
 431 cline in the 850 hPa geopotential height offshore Atacama (Fig. 9c) that reinforces northerly
 432 winds along the western coast of South America due to increased zonal pressured gra-
 433 dient (Fig. 10b), enhancing moisture transport from the tropics in the lower free tropo-
 434 sphere and leading to a positive trend in specific humidity at 850 hPa (Fig. 9d). The
 435 warm trend in the SST offshore Atacama is spatially much more limited (Fig. 9e) than
 436 the general increase in TCWV. We suspect that this trend is potentially moistening the
 437 MBL (Fig. 10a), although other factors may play a role (e.g., weaker southerly winds,
 438 Fig. 10b).

439 The negative trend in the form of the 850 hPa low-pressure off the coast of Ata-
 440 cama is a somewhat curious feature, considering that most of the subtropical and mid-
 441 latitude regions exhibit a marked positive trend in the geopotential height and sea level
 442 pressure as a consequence of global warming (Fig. 9c,f, and e.g., Gillett & Stott, 2009).
 443 However, we suspect that both factors are linked. The poleward displacement of the sub-
 444 tropical jet due to the Hadley cell expansion (Lu et al., 2007) allows a more frequent for-
 445 mation of the BH in the upper troposphere at the synoptic scale as proposed by Garreaud

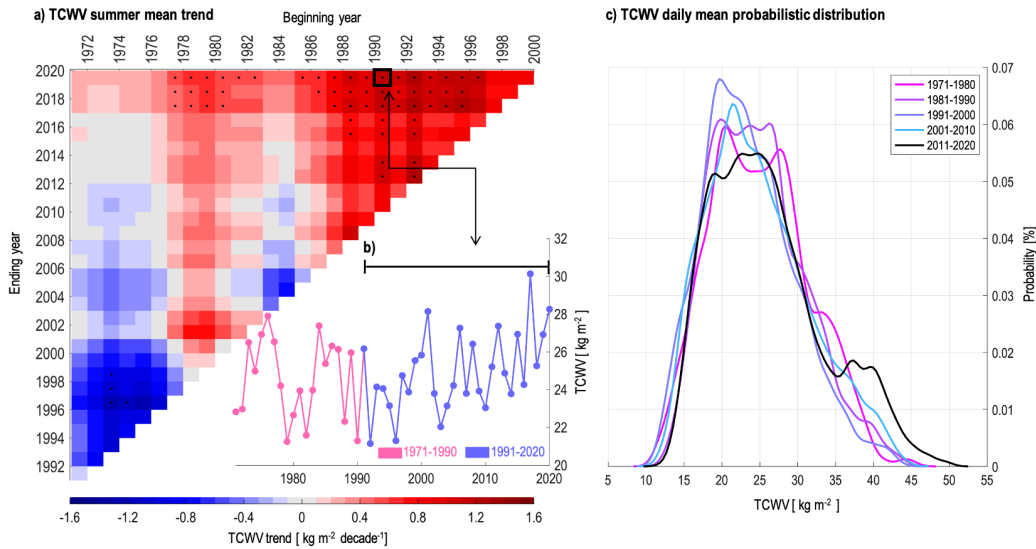


Figure 8. (a) Heatmap of the multi-trend analysis of TCWV summer mean (December–March) for a box offshore Atacama (18–23°S, 74–71°W) for different periods starting in 1971 and ending in 2020. Significance at 95% is marked with a black dot in the center of the box. (b) Time series of summer TCWV from 1971–2020 averaged for the same box offshore Atacama. The blue time series corresponds to the period 1991–2020, highlighted in the heatmap with a black square. (c) The probability density of daily means of summer TCWV in the same Atacama offshore region for different decades (colored lines). TCWV is obtained from ERA5.

446 (1999). As discussed in the previous section, the anomalous poleward displaced BH is
 447 conducive to forming the 850 hPa low-pressure offshore Atacama.

448 Additionally, the expansion of the Hadley cell results in a shift of the SEPA towards
 449 the pole, relaxing the pressure gradient along the west coast of South America and po-
 450 tentially helping the low pressure to form. The tropical expansion has been linked to global
 451 warming induced by greenhouse gases (GHG) forcing (Lu et al., 2007), but other fac-
 452 tors may also play a role. For example, the positive trend in the Southern Annular Mode
 453 (SAM, Marshall, 2003), in which the polar jet weakens and displaced poleward, espe-
 454 cially in austral summer (Fogt & Marshall, 2020), help to displace the southern edge of
 455 the SEPA poleward. This trend is partially linked to the stratospheric ozone loss, with
 456 GHG and tropical variability playing secondary roles (Fogt & Marshall, 2020). There-
 457 fore, it is highly likely that the observed trend in moisture and circulation along the west
 458 coast of South America results from several processes occurring at different time scales,
 459 conspiring to produce a generalized increase in humidity transport to the Atacama Desert.

460 The MN episodes were identified in this study using a set of four weather stations
 461 located in the hyperarid core. Nevertheless, we suspect that the MN can have an influ-
 462 ence beyond this region. As few precipitation measurements exist in the Atacama, the
 463 presence of vegetation could serve as an indirect proxy for past changes in the rainfall
 464 regime. For example, the blooming desert or “desierto florido” is frequently observed in
 465 Southern Atacama (25–30°S) and is a good tracer of winter rainfall episodes. Similarly,
 466 Chávez et al. (2019) found the first evidence of a “pre-Andean blooming desert”, trig-
 467 gered by an anomalous wet summer in 2012 in the precordillera. This anomalous bloom-
 468 ing was only observed recently despite research spanning from 1981 to 2015. This aligns
 469 well with a wet year in the hyperarid core with at least four rainy days related to MNs

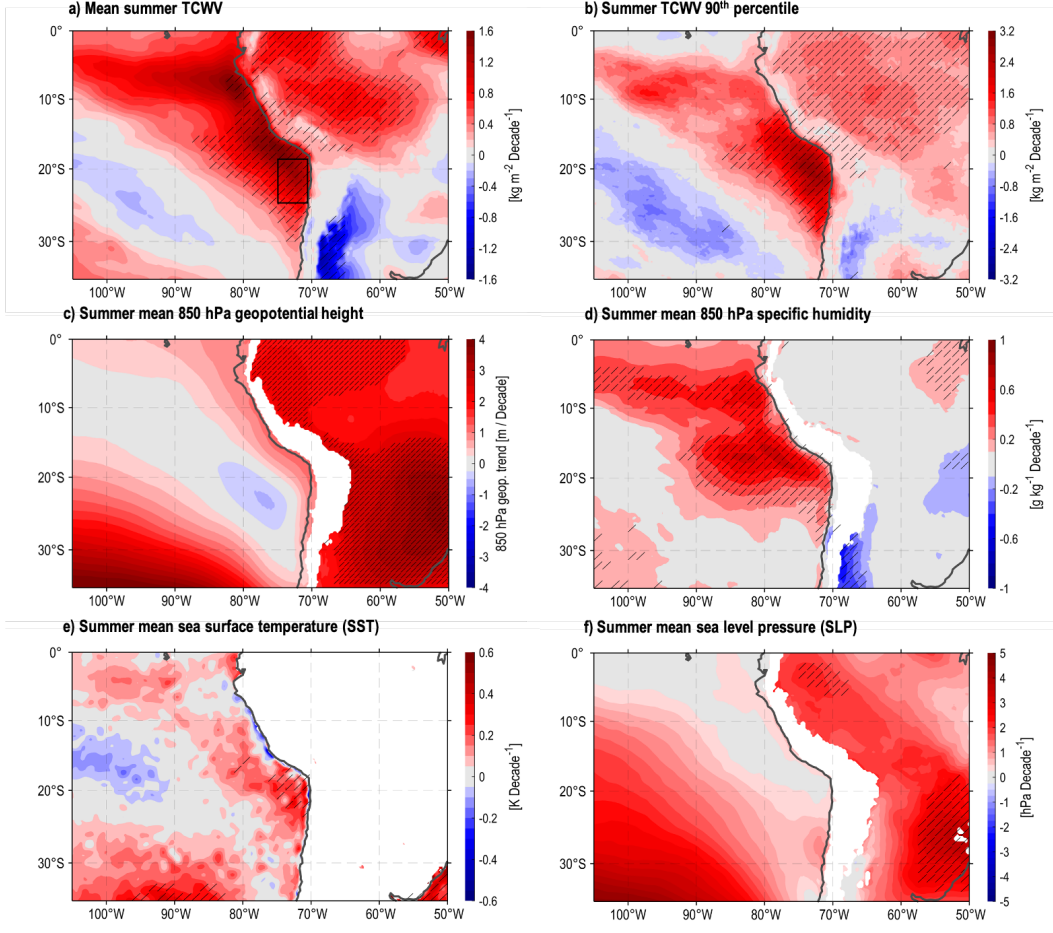


Figure 9. Linear trend (1991-2020) for summer (December-March) of (a) mean TCWV, (b) summer 90th percentile, (c) mean 850 hPa geopotential height, (d) mean 850 hPa specific humidity, (e) mean SST and (f) sea level pressure. Areas with black stripes indicate statistical significance of 95% of confidence level. In panels c, d, e, and f, the Andes cordillera is patched white for altitudes above 850 hPa. Data from ERA5.

470 (Fig.4a). The blooming seems to be part of a greater greening pattern affecting eastern
 471 Atacama. Lepage et al. (2023) found a marked positive trend of the normalized differ-
 472 ence vegetation index (NDVI) between 2000–2020 in a greening strip between Southern
 473 Perú and Northern Chile (7.5–22.5°S). As the greening is so extended, it is unlikely to
 474 be linked to land-use changes. We propose that the more frequent MN mechanism off-
 475 shore Atacama observed in the last decades complements the classic easterly moisture
 476 source for summer storms, increasing moisture availability on the eastern edge of the At-
 477 acama and the precordillera, and inducing more frequent precipitation. The increased
 478 moisture advected from the coast into the desert matches with recent estimations of rel-
 479 atively high fog frequency in the precordillera (Böhm et al., 2021), which could further
 480 provide water to vegetation.

481 **4 Summary and conclusions**

482 We have investigated summer rainfall episodes in the Atacama Desert using a case
 483 study and a composite analysis from reanalysis ERA5, high-resolution WRF simulations,

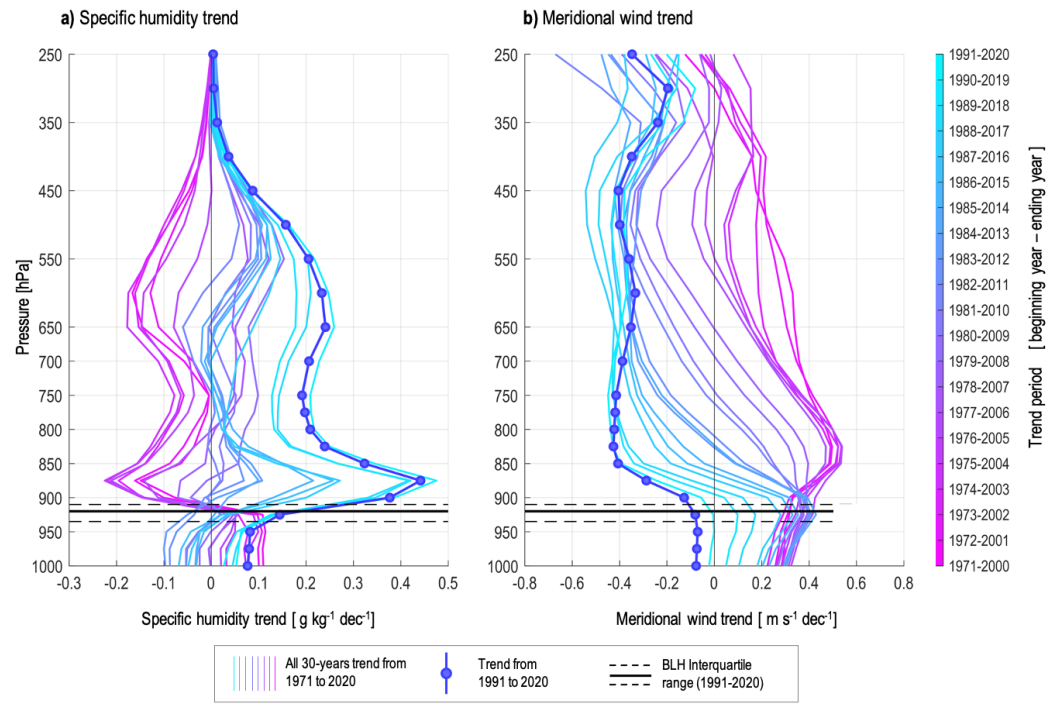


Figure 10. Vertical profiles of austral summer of (a) specific humidity trend and (b) meridional wind linear trend for 30 years period (colored lines) for the Atacama offshore region (18–23°S, 74–71°W). The blue dotted line corresponds to the 1991–2020 trend. We included the interquartile range of the boundary layer height (BLH, dashed thin black line) and the mean (thick black line) for the period 1991–2020. Data from ERA5.

484 surface observations, satellites, and remote sensing. Around 75% of rainfall days and 65%
 485 of total rainfall in summer in the hyperarid core of the Atacama are triggered by mois-
 486 ture coming from the Pacific. We called these episodes Moist Northerlies (MNs), asso-
 487 ciated with an anomalous southward displaced BH and a trough anomaly in the upper
 488 troposphere over the southeast Pacific. This upper-troposphere dipole is conducive to
 489 forming a non-frontal low-pressure system at 850 hPa offshore Perú and northern Chile.
 490 In the forefront of the low pressure, an atmospheric river-like structure transports the
 491 moisture from the tropical eastern Pacific to the south. This produces a marked increase
 492 in TCWV offshore Atacama, reaching extreme values (up to $\sim 55 \text{ kg m}^{-2}$) that are typi-
 493 cally observed over the Amazon basin.

494 Based on a case study, we found that the classic Rutlant Cell that brings dry air
 495 from the subsidence region along the west coast of South America to the Andes is also
 496 a moist circulation, pumping the moisture-enriched air from the lower free-troposphere
 497 offshore Atacama to the interior. Surface-specific humidity can increase from 3 to 12 g kg^{-1}
 498 in the hyperid core and precordillera during the rainfall episode. The topographic
 499 uplift triggers clouds along the precordillera, mainly as stratus clouds but with some cum-
 500ulonimbus embedded. Part of the moisture can reach the Altiplano and serve as a source
 501 for the evening thunderstorms. Mid-troposphere easterly winds at night bring clouds to
 502 the pampas and the coast. Evidence from 72 rainfall episodes in the Atacama shows that
 503 this mechanism produces mainly light rain during the night (03–09 LT), although rain
 504 can occur at any time of the day. The MNs affect mostly the northern part of the desert

505 (i.e., Arica), the east (i.e., Quillagua and Calama), and decrease its influence to the south
506 (i.e., Antofagasta).

507 Most of the MN rainfall episodes occur during the neutral or weak La Niña con-
508 ditions in the Central Pacific, and during the phases 7-8-1 of the MJO. These large-scale
509 oscillations are conducive to weakening the subtropical jet and producing the upper-troposphere
510 dipole over the Southeast Pacific that is required to form the 850 hPa low-pressure sys-
511 tem. Our results suggest that this mechanism is driven mainly by atmospheric dynam-
512 ics and not by changes in local SST offshore Atacama. In fact, warmer than normal SST
513 anomalies over the Southeast Pacific accompanying the MN episodes seem to be a con-
514 sequence of the general weakening of the SEPA rather than a triggering mechanism of
515 the MNs and the precipitation.

516 Finally, a trend analysis highlights that the MNs have become more frequent within
517 the last ~ 30 years, further enhancing extreme values of TCWV offshore Atacama. This
518 extra moisture supply explains the increase in MN rainfall episodes in the last decades
519 in the northern and eastern Atacama, the general wet trend across much of southern Perú
520 and Northern Chile, and the greening in the precordillera. Further measurements are needed
521 to correctly understand how Pacific-originate westerly moisture is transported inland,
522 considering the region’s complex topography. Future works must address the impact of
523 the Hadley cell expansion, GHG, and SAM on the MN rainfall mechanism accurately.
524 For example, statistically downscaled climate projections show increased summer rain-
525 fall in the Atacama under different future global warming scenarios (Araya-Osses et al.,
526 2020). We suspect that this increased summer rainfall could be influenced by enhanced
527 MN configuration. Furthermore, wetter conditions during globally warmer climates in
528 the past (e.g., Holocene and Pleistocene) have mainly been linked to enhanced periods
529 of El Niño in the Equatorial Pacific and its impact on winter rainfall (Ritter et al., 2019;
530 González-Pinilla et al., 2021) may also be partially influenced by the rising frequency of
531 MN episodes in summer, a neutral-cold ENSO induced mechanism.

532 Open Research Section

533 ERA5 data (Hersbach et al., 2020) were downloaded from the Copernicus Climate
534 Data Store (CDS) via <https://cds.climate.copernicus.eu/>. Data from WRF sim-
535 ulation can be obtained from the CRC1211 database via [https://www.crc1211db.uni-](https://www.crc1211db.uni-koeln.de/)
536 [http://www.cr2.cl/datos-de-](http://www.cr2.cl/datos-de-precipitacion/)
537 <https://climatologia.meteochile.gob.cl> and (3) DGA,
538 <https://dga.mop.gob.cl>. ENSO index can be downloaded via [https://www.cpc.ncep](https://www.cpc.ncep.noaa.gov/data/indices)
539 [.noaa.gov/data/indices](https://www.ps1.noaa.gov/mjo/mjoindex/). MJO index can be downloaded via [https://www.ps1.noaa](https://www.ps1.noaa.gov/mjo/mjoindex/)
540 [.gov/mjo/mjoindex/](https://worldview.earthdata.nasa.gov). We acknowledge the use of imagery from the NASA Worldview
541 application (<https://worldview.earthdata.nasa.gov>), part of the NASA Earth Ob-
542 serving System Data and Information System (EOSDIS).

543 Acknowledgments

544 We gratefully acknowledge financial support by the Deutsche Forschungsgemeinschaft
545 (DFG, German Research Foundation)–Projektnummer 268236062-SFB 1211.

546 References

- 547 Araya-Osses, D., Casanueva, A., Román-Figueroa, C., Uribe, J. M., & Paneque, M.
548 (2020). Climate change projections of temperature and precipitation in Chile
549 based on statistical downscaling. *Climate Dynamics*, *54*, 4309–4330. doi:
550 <https://doi.org/10.1007/s00382-020-05231-4>
551 Barrett, B., Campos, D., Vicencio, J., & Rondanelli, R. (2016). Extreme temper-
552 ature and precipitation events in March 2015 in central and northern Chile.

- 553 *Journal of Geophysical Research: Atmospheres*, 121(9), 4563–4580.
- 554 Böhm, C., Schween, J. H., Reyers, M., Maier, B., Löhnert, U., & Crewell, S.
555 (2021). Toward a Climatology of Fog Frequency in the Atacama Desert
556 via Multispectral Satellite Data and Machine Learning Techniques. *Jour-*
557 *nal of Applied Meteorology and Climatology*, 60(8), 1149–1169. doi:
558 <https://doi.org/10.1175/JAMC-D-20-0208.1>
- 559 Bozkurt, D., Rondanelli, R., Garreaud, R., & Arriagada, A. (2016). Impact of
560 Warmer Eastern Tropical Pacific SST on the March 2015 Atacama Floods.
561 *Monthly Weather Review*, 144(11), 4441–4460.
- 562 Böhm, C., Reyers, M., Knarr, L., & Crewell, S. (2021). The role of moisture con-
563 veyor belts for precipitation in the Atacama Desert. *Geophysical Research Let-*
564 *ters*, 48(24), e2021GL094372. doi: <https://doi.org/10.1029/2021GL094372>
- 565 Chávez, R., Moreira-Muñoz, A., Galleguillos, M., Olea, M., Aguayo, J., Latín, A., . . .
566 Manríquez, H. (2019). GIMMS NDVI time series reveal the extent, duration,
567 and intensity of “blooming desert” events in the hyper-arid Atacama Desert,
568 Northern Chile. *International Journal of Applied Earth Observation and*
569 *Geoinformation*, 76, 193–203. doi: <https://doi.org/10.1016/j.jag.2018.11.013>
- 570 Demortier, A., Bozkurt, D., & Jacques-Coper, M. (2021). Identifying key driving
571 mechanisms of heat waves in central Chile. *Climate Dynamics*, 57(9–10), 2415–
572 2432. doi: <https://doi.org/10.1007/s00382-021-05810-z>
- 573 Dunai, T. J., Melles, M., Quandt, D., Knief, C., & Amelung, W. (2020). Whitepa-
574 per: Earth – evolution at the dry limit. *Global and Planetary Change*, 193,
575 103275. doi: <https://doi.org/10.1016/j.gloplacha.2020.103275>
- 576 Fogt, R. L., & Marshall, G. J. (2020). The Southern Annular Mode: variability,
577 trends, and climate impacts across the Southern Hemisphere. *Wiley Interdisci-*
578 *plinary Reviews: Climate Change*, 11(4), e652. doi: <https://doi.org/10.1002/wcc.652>
- 579
- 580 Garreaud, R. (1999). Multiscale Analysis of the Summertime Precipitation over the
581 Central Andes. *Monthly Weather Review*, 127(5), 901 - 921. doi: [https://doi](https://doi.org/10.1175/1520-0493(1999)127<0901:MAOTSP>2.0.CO;2)
582 [.org/10.1175/1520-0493\(1999\)127<0901:MAOTSP>2.0.CO;2](https://doi.org/10.1175/1520-0493(1999)127<0901:MAOTSP>2.0.CO;2)
- 583 Garreaud, R., & Aceituno, P. (2001). Interannual Rainfall Variability over the South
584 American Altiplano. *Journal of Climate*, 14(12), 2779 - 2789. doi: [https://doi](https://doi.org/10.1175/1520-0442(2001)014<2779:IRVOTS>2.0.CO;2)
585 [.org/10.1175/1520-0442\(2001\)014<2779:IRVOTS>2.0.CO;2](https://doi.org/10.1175/1520-0442(2001)014<2779:IRVOTS>2.0.CO;2)
- 586 Garreaud, R., Vuille, M., & Clement, A. (2003). The climate of the Altiplano: ob-
587 served current conditions and mechanisms of past changes. *Palaeogeography,*
588 *palaeoclimatology, palaeoecology*, 194(1–3), 5–22.
- 589 Gillett, N., & Stott, P. (2009). Attribution of anthropogenic influence on seasonal
590 sea level pressure. *Geophysical Research Letters*, 36(23). doi: [https://doi.org/](https://doi.org/10.1029/2009GL041269)
591 [10.1029/2009GL041269](https://doi.org/10.1029/2009GL041269)
- 592 González-Pinilla, F. J., Latorre, C., Rojas, M., Houston, J., Rocuant, M. I., Mal-
593 donado, A., . . . Betancourt, J. L. (2021). High-and low-latitude forcings
594 drive Atacama Desert rainfall variations over the past 16,000 years. *Science*
595 *Advances*, 7(38), eabg1333. doi: 10.1126/sciadv.abg1333
- 596 Guan, B., & Waliser, D. (2015). Detection of atmospheric rivers: Evaluation and ap-
597 plication of an algorithm for global studies. *Journal of Geophysical Research -*
598 *Atmospheres*, 120(24), 12514–12535.
- 599 Heidinger, H., Carvalho, L., Jones, C., Posadas, A., & Quiroz, R. (2018). A new
600 assessment in total and extreme rainfall trends over central and southern Pe-
601 ruvian Andes during 1965–2010. *International Journal of Climatology*, 38,
602 e998–e1015. doi: <https://doi.org/10.1002/joc.5427>
- 603 Hersbach, H., Bell, B., Berrisford, P., Hirahara, S., Horányi, A., Muñoz-Sabater,
604 J., . . . Thépaut, J.-N. (2020). The ERA5 global reanalysis. *Quarterly*
605 *Journal of the Royal Meteorological Society*, 146(730), 1999–2049. doi:
606 <https://doi.org/10.1002/qj.3803>
- 607 Hoffmeister, D. (2018). Meteorological and soil measurements of the permanent

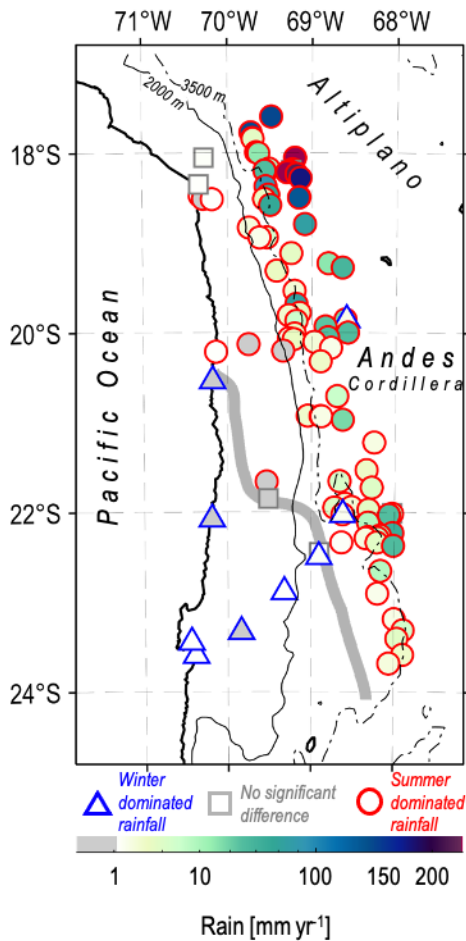
- 608 weather stations in the Atacama desert, Chile. *CRC1211 Database*. Retrieved
 609 from <https://www.crc1211db.uni-koeln.de/DOI/doi.php?doiID=1>
- 610 Houston, J., & Hartley, A. J. (2003). The central Andean west-slope rainshadow
 611 and its potential contribution to the origin of hyper-aridity in the Atacama
 612 Desert. *International Journal of Climatology*, *23*(12), 1453–1464. doi:
 613 10.1002/joc.938
- 614 Huang, B., Thorne, P. W., Banzon, V. F., Boyer, T., Chepurin, G., Lawrimore,
 615 J. H., ... Zhang, H.-M. (2017). Extended reconstructed sea surface tem-
 616 perature, version 5 (ERSSTv5): upgrades, validations, and intercomparisons.
 617 *Journal of Climate*, *30*(20), 8179–8205.
- 618 Jacques-Coper, M., Veloso-Aguila, D., Segura, C., & Valencia, A. (2021). Intra-
 619 seasonal teleconnections leading to heat waves in central Chile. *International*
 620 *Journal of Climatology*, *41*(9), 4712–4731. doi: [https://doi.org/10.1002/](https://doi.org/10.1002/joc.7096)
 621 [joc.7096](https://doi.org/10.1002/joc.7096)
- 622 Jordan, T. E., Herrera, C., Godfrey, L. V., Colucci, S. J., Gamboa, C., Urrutia, J.,
 623 ... Paul, J. F. (2019). Isotopic characteristics and paleoclimate implications
 624 of the extreme precipitation event of March 2015 in northern Chile. *Andean*
 625 *Geology*, *46*(1), 1–31. doi: <https://doi.org/10.5027/andgeoV46n1-3087>
- 626 Lepage, H. V., Barnes, E., Kor, E., Hunter, M., & Barnes, C. H. (2023). Greening
 627 and Browning Trends on the Pacific Slope of Peru and Northern Chile. *Remote*
 628 *Sensing*, *15*(14), 3628. doi: <https://doi.org/10.3390/rs15143628>
- 629 Lu, J., Vecchi, G. A., & Reichler, T. (2007). Expansion of the Hadley cell under
 630 global warming. *Geophysical Research Letters*, *34*(6). doi: [https://doi.org/10](https://doi.org/10.1029/2006GL028443)
 631 [.1029/2006GL028443](https://doi.org/10.1029/2006GL028443)
- 632 L’Heureux, M. L., Collins, D. C., & Hu, Z.-Z. (2013). Linear trends in sea sur-
 633 face temperature of the tropical Pacific Ocean and implications for the El
 634 Niño-Southern Oscillation. *Climate Dynamics*, *40*(5-6), 1223–1236. doi:
 635 <https://doi.org/10.1007/s00382-012-1331-2>
- 636 Madden, R., & Julian, P. (1972). Description of global-scale circulation cells in the
 637 tropics with a 40–50-day period. *J. Atmos. Sci.*, *29*, 1109–1123. doi: [https://](https://doi.org/10.1175/1520-0469(1972)029<1109:DOGSCC>2.0.CO;2)
 638 [doi.org/10.1175/1520-0469\(1972\)029<1109:DOGSCC>2.0.CO;2](https://doi.org/10.1175/1520-0469(1972)029<1109:DOGSCC>2.0.CO;2)
- 639 Marshall, G. J. (2003). Trends in the Southern Annular Mode from observations
 640 and reanalyses. *Journal of climate*, *16*(24), 4134–4143. doi: [https://doi.org/10](https://doi.org/10.1175/1520-0442(2003)016(4134:TITSAM)2.0.CO;2)
 641 [.1175/1520-0442\(2003\)016\(4134:TITSAM\)2.0.CO;2](https://doi.org/10.1175/1520-0442(2003)016(4134:TITSAM)2.0.CO;2)
- 642 Meseguer-Ruiz, O., Cortesi, N., Guijarro, J. A., & Sarricolea, P. (2020). Weather
 643 regimes linked to daily precipitation anomalies in Northern Chile. *Atmospheric*
 644 *Research*, *236*, 104802. doi: <https://doi.org/10.1016/j.atmosres.2019.104802>
- 645 Olivares, M. (2020). Caracterización climatológica de la precipitación en temporada
 646 estival en la zona norte de Chile considerando el periodo entre los años 1990 y
 647 2019. *Stratus*, 1-35. Retrieved from [https://revistastratus.meteochile](https://revistastratus.meteochile.gob.cl/index.php/2020/12/01/caracterizacion-climatologica-de-la-precipitacion-en-temporada-estival-en-la-zona-norte-de-chile-considerando-el-periodo-entre-los-anos-1990-y-2019/)
 648 [.gob.cl/index.php/2020/12/01/caracterizacion-climatologica-de](https://revistastratus.meteochile.gob.cl/index.php/2020/12/01/caracterizacion-climatologica-de-la-precipitacion-en-temporada-estival-en-la-zona-norte-de-chile-considerando-el-periodo-entre-los-anos-1990-y-2019/)
 649 [-la-precipitacion-en-temporada-estival-en-la-zona-norte-de-chile](https://revistastratus.meteochile.gob.cl/index.php/2020/12/01/caracterizacion-climatologica-de-la-precipitacion-en-temporada-estival-en-la-zona-norte-de-chile-considerando-el-periodo-entre-los-anos-1990-y-2019/)
 650 [-considerando-el-periodo-entre-los-anos-1990-y-2019/](https://revistastratus.meteochile.gob.cl/index.php/2020/12/01/caracterizacion-climatologica-de-la-precipitacion-en-temporada-estival-en-la-zona-norte-de-chile-considerando-el-periodo-entre-los-anos-1990-y-2019/)
- 651 Reyers, M. (2018). *WRF output daily accumulated total precipitation 10 km reso-*
 652 *lution Atacama* [dataset]. CRC1211 Database (CRC1211DB). Retrieved from
 653 [https://doi.org.10.5880/CRC1211DB.20](https://doi.org/10.5880/CRC1211DB.20)
- 654 Reyers, M., Böhm, C., Knarr, L., Shao, Y., & Crewell, S. (2020). Synoptic-to-
 655 regional scale analysis of rainfall in the Atacama Desert (18S–26S) using a
 656 long-term simulation with WRF. *Monthly Weather Review*, *149*(1), 91–112.
 657 doi: <https://doi.org/10.1175/MWR-D-20-0038.1>
- 658 Reyers, M., & Shao, Y. (2019). Cutoff lows off the coast of the Atacama Desert un-
 659 der present day conditions and in the Last Glacial Maximum. *Global and Plan-*
 660 *etary Change*, *181*, 102983.
- 661 Ritter, B., Wennrich, V., Medialdea, A., Brill, D., King, G., Schneiderwind, S.,
 662 ... others (2019). Climatic fluctuations in the hyperarid core of the At-

- 663 acama Desert during the past 215 ka. *Scientific reports*, 9(1), 5270. doi:
 664 <https://doi.org/10.1038/s41598-019-41743-8>
- 665 Rondanelli, R., Hatchett, B., Rutllant, J., Bozkurt, D., & Garreaud, R. (2019).
 666 Strongest MJO on record triggers extreme Atacama rainfall and warmth
 667 in Antarctica. *Geophysical Research Letters*, 46(6), 3482–3491. doi:
 668 <https://doi.org/10.1029/2018GL081475>
- 669 Rondanelli, R., Molina, A., & Falvey, M. (2015). The Atacama Surface Solar Max-
 670 imum. *Bulletin of the American Meteorological Society*, 96(3), 405 - 418. doi:
 671 [10.1175/BAMS-D-13-00175.1](https://doi.org/10.1175/BAMS-D-13-00175.1)
- 672 Rose, T., Crewell, S., Löhnert, U., & Simmer, C. (2005). A network suit-
 673 able microwave radiometer for operational monitoring of the cloudy atmo-
 674 sphere. *Atmospheric Research*, 75(3), 183-200. (CLIWA-NET: Observa-
 675 tion and Modelling of Liquid Water Clouds) doi: [https://doi.org/10.1016/](https://doi.org/10.1016/j.atmosres.2004.12.005)
 676 [j.atmosres.2004.12.005](https://doi.org/10.1016/j.atmosres.2004.12.005)
- 677 Rutllant, J., Muñoz, R., & Garreaud, R. (2013). Meteorological observations on
 678 the northern Chilean coast during VOCALS-REx. *Atmospheric Chemistry and*
 679 *Physics*, 13(6), 3409–3422.
- 680 Schween, J. H., del Rio, C., García, J.-L., Osses, P., Westbrook, S., & Löhnert, U.
 681 (2022). Life Cycle of Stratocumulus Clouds over one Year at the Coast of the
 682 Atacama Desert. *Atmospheric Chemistry and Physics Discussions*, 2022, 1–33.
 683 doi: [10.5194/acp-2022-108](https://doi.org/10.5194/acp-2022-108)
- 684 Schween, J. H., Hoffmeister, D., & Löhnert, U. (2020). Filling the observational
 685 gap in the Atacama Desert with a new network of climate stations. *Global and*
 686 *Planetary Change*, 184, 103034. doi: <https://doi.org/10.1016/j.gloplacha.2019>
 687 [.103034](https://doi.org/10.1016/j.gloplacha.2019.103034)
- 688 Skamarock, W. C., Klemp, J. B., Dudhia, J., Gill, D. O., Barker, D. M., Duda,
 689 M. G., ... others (2008). A description of the advanced research WRF version
 690 3. *NCAR technical note*, 475, 113.
- 691 Valdivielso, S., Vázquez-Suñé, E., & Custodio, E. (2020). Origin and vari-
 692 ability of oxygen and hydrogen isotopic composition of precipitation in
 693 the Central Andes: A review. *Journal of Hydrology*, 587, 124899. doi:
 694 <https://doi.org/10.1016/j.jhydrol.2020.124899>
- 695 Vicencio, J. (2021). Analysis of an extreme precipitation event in the Atacama
 696 Desert on January 2020 and its relationship to humidity advection along the
 697 Southeast Pacific. *Atmósfera*, 35(3), 421-448. doi: [https://doi.org/10.20937/](https://doi.org/10.20937/ATM.52911)
 698 [ATM.52911](https://doi.org/10.20937/ATM.52911)
- 699 Vicencio Veloso, J., Böhm, C., Schween, J. H., Löhnert, U., & Crewell, S. (2024).
 700 A comparative study of the atmospheric water vapor in the Atacama
 701 and Namib Desert. *Global and Planetary Change*, 232, 104320. doi:
 702 <https://doi.org/10.1016/j.gloplacha.2023.104320>
- 703 Vuille, M., Hardy, D. R., Braun, C., Keimig, F., & Bradley, R. S. (1998). Atmo-
 704 spheric circulation anomalies associated with 1996/1997 summer precipitation
 705 events on Sajama Ice Cap, Bolivia. *Journal of Geophysical Research: Atmo-*
 706 *spheres*, 103(D10), 11191–11204.
- 707 Wang, S., Martin, Z. K., Sobel, A. H., Tippett, M. K., Dias, J., Kiladis, G. N., ...
 708 Wu, J. (2022). A multivariate index for tropical intraseasonal oscillations
 709 based on the seasonally-varying modal structures. *Journal of Geophysical Re-*
 710 *search: Atmospheres*, 127(4), e2021JD035961. (e2021JD035961 2021JD035961)
 711 doi: <https://doi.org/10.1029/2021JD035961>
- 712 Welp, L. R., Olson, E. J., Valdivia, A. L., Larico, J. R., Arhuire, E. P., Paredes,
 713 L. M., ... Michalski, G. M. (2022). Reinterpreting Precipitation Stable Water
 714 Isotope Variability in the Andean Western Cordillera Due To Sub-Seasonal
 715 Moisture Source Changes and Sub-Cloud Evaporation. *Geophysical Research*
 716 *Letters*, 49(18), e2022GL099876. doi: <https://doi.org/10.1029/2022GL099876>
- 717 Wennrich, V., Böhm, C., Brill, D., Carballeira, R., Hoffmeister, D., Jaeschke, A., ...

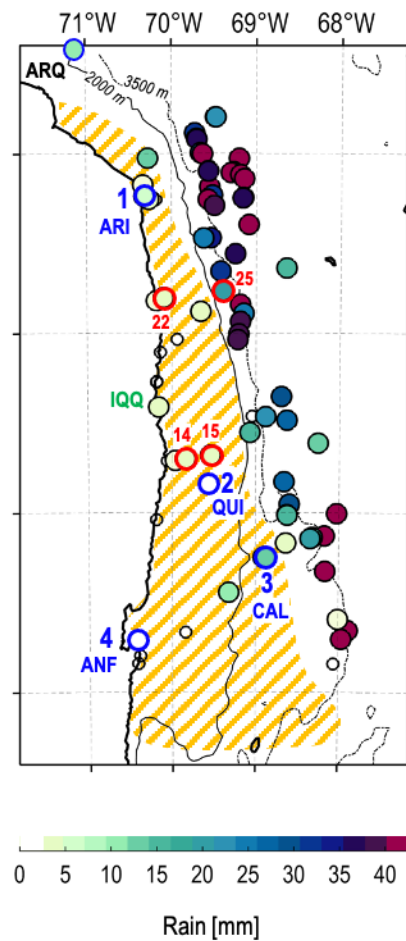
718 Melles, M. (2024). Late Pleistocene to modern precipitation changes at the
719 Paranal clay pan, central Atacama Desert. *Global and Planetary Change*, 233,
720 104349. doi: <https://doi.org/10.1016/j.gloplacha.2023.104349>

Figure 1.

a) Climatology of summer rainfall



b) Accumulated rainfall 28-31/01/2019



c) 3-hourly rainfall from 28/01 to 31/01/2019

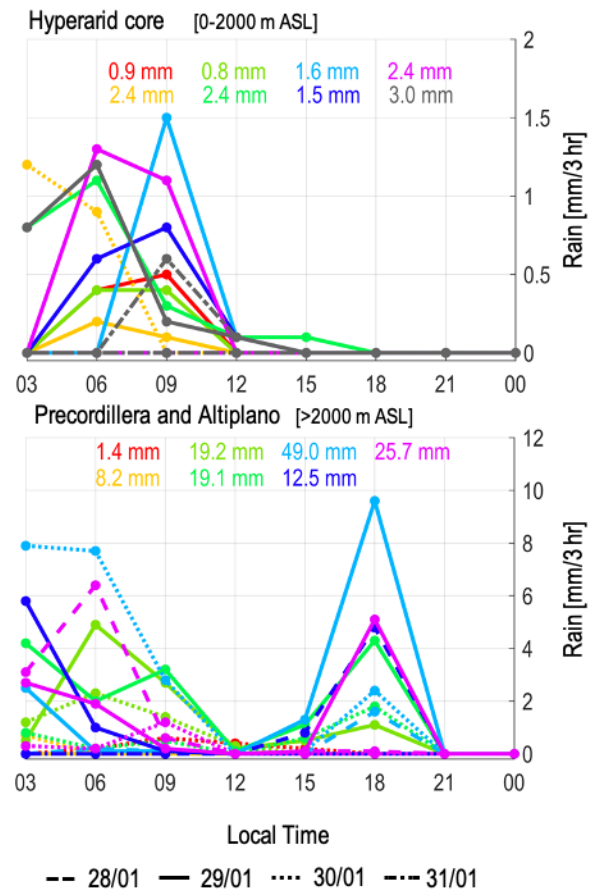


Figure 2.

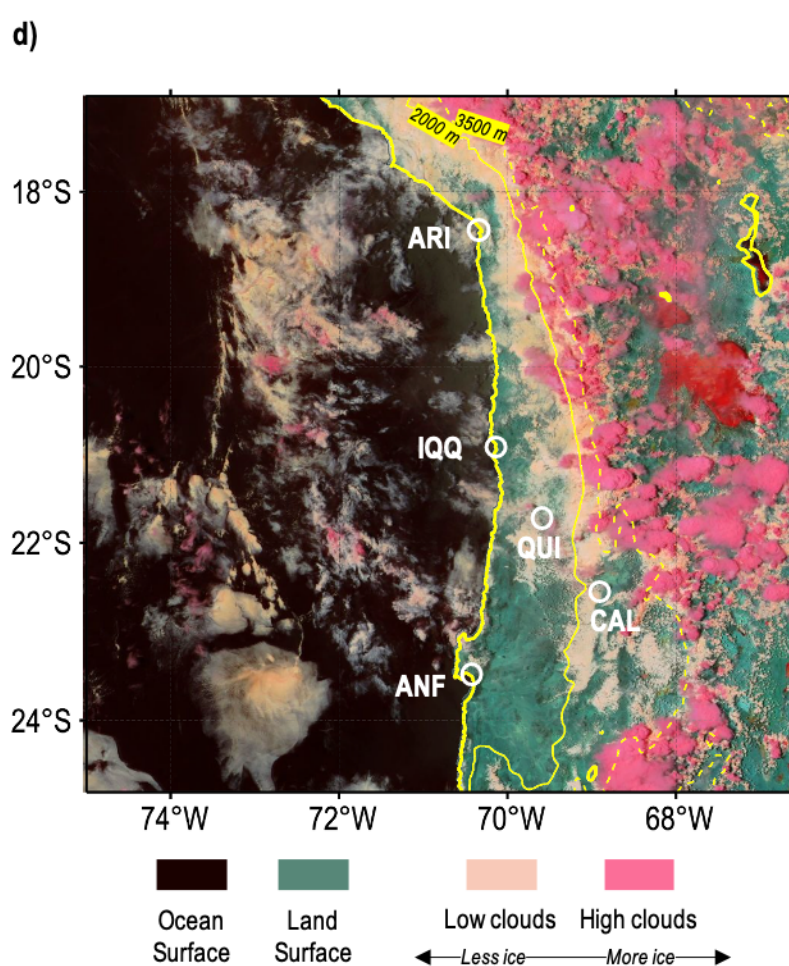
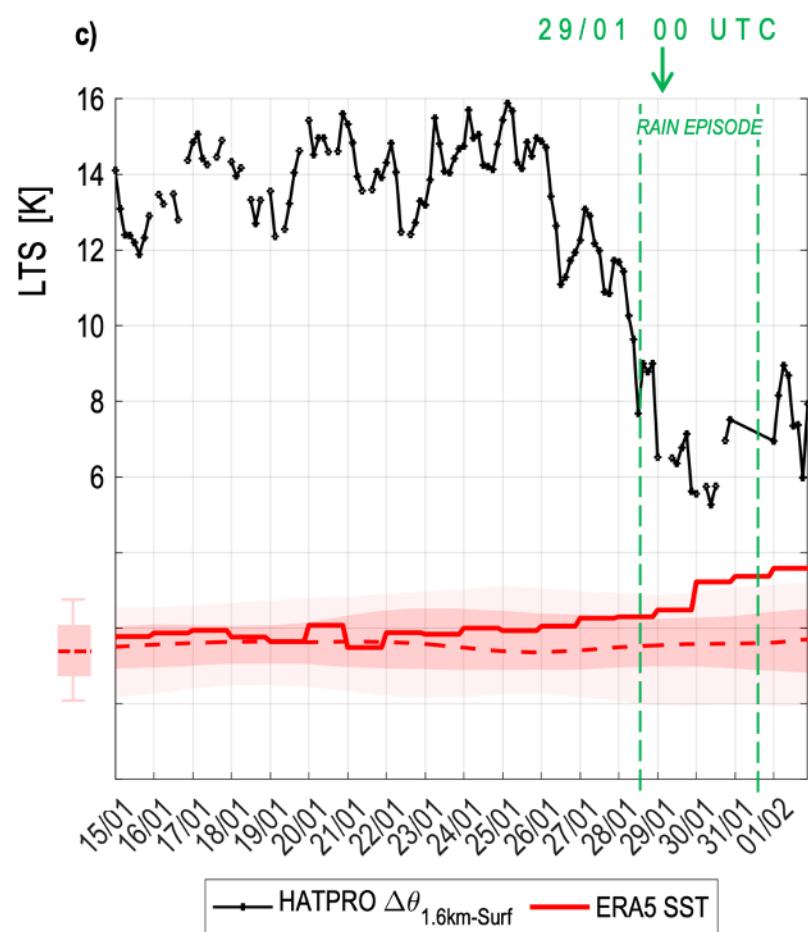
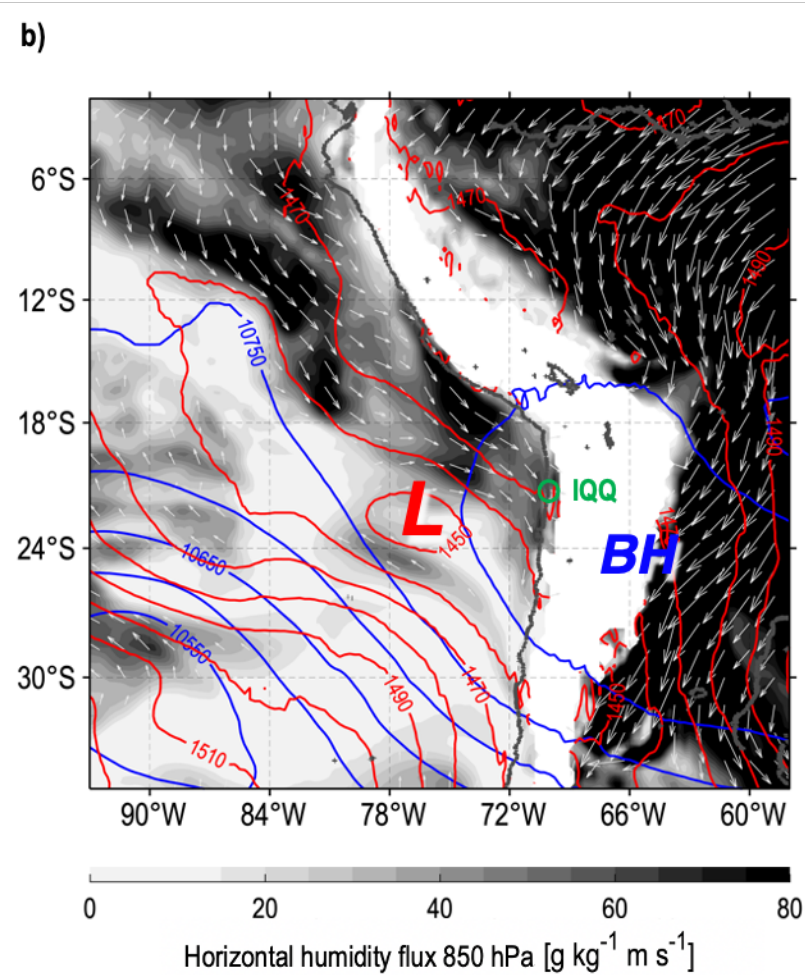
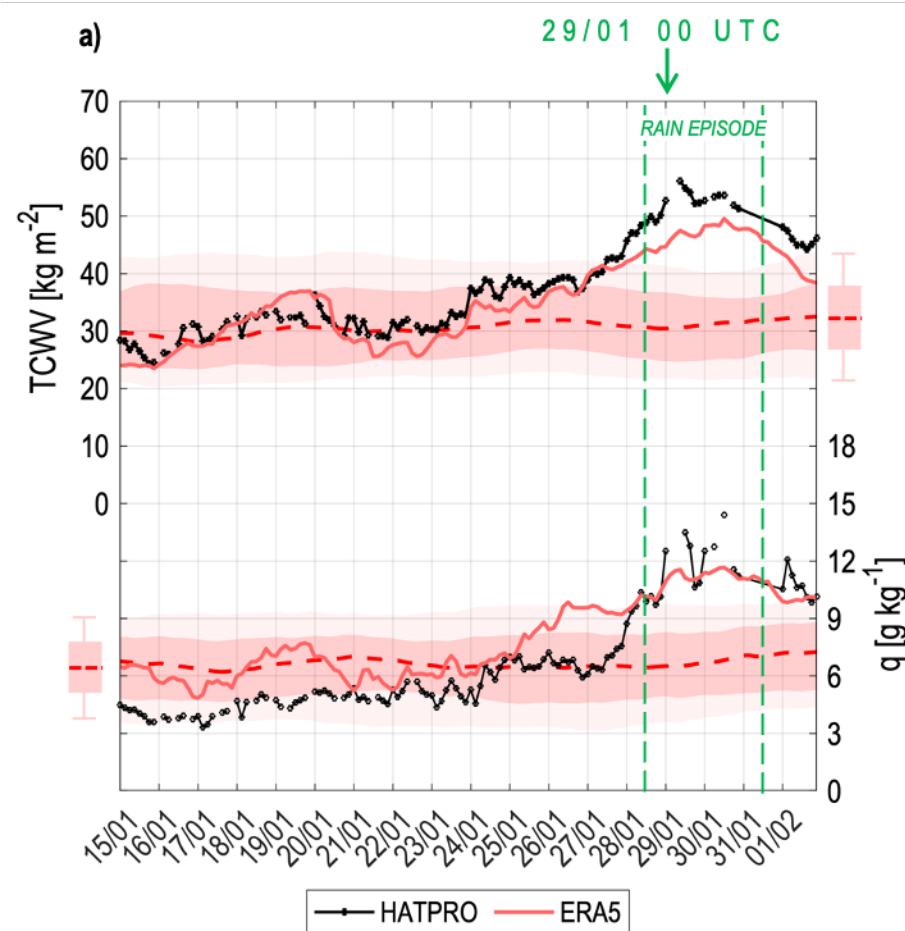
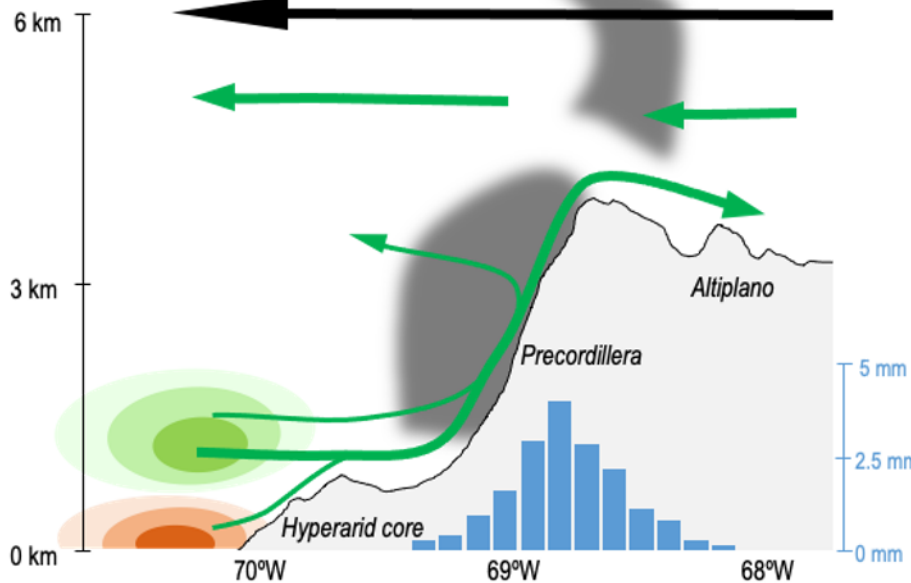
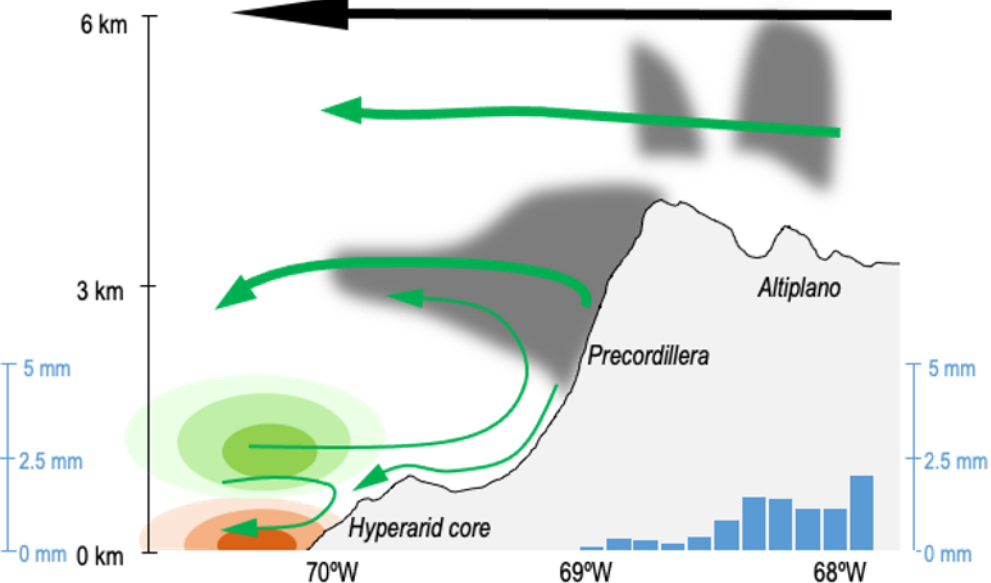


Figure 3.

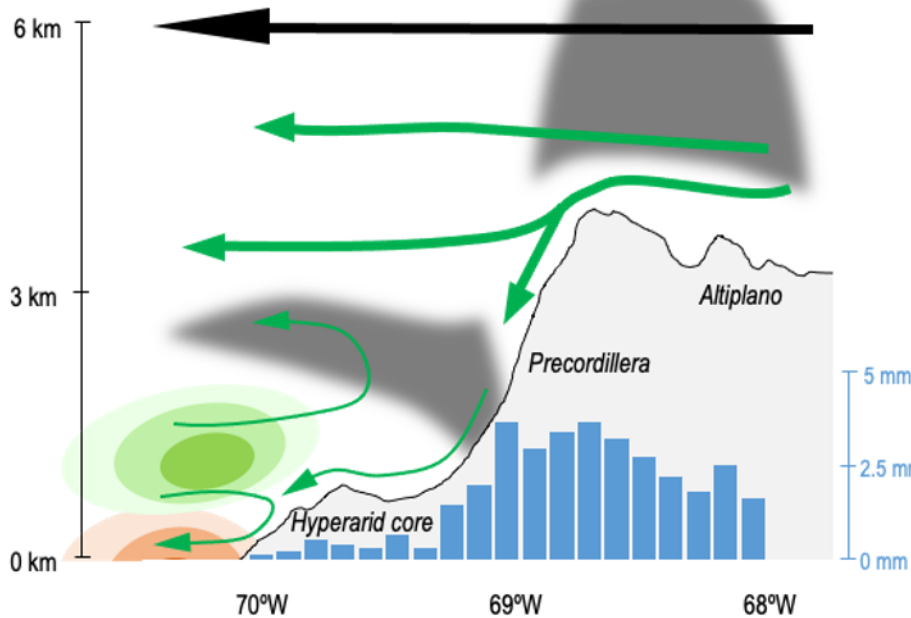
a) Afternoon 12-18 LT



b) Evening 18-00 LT



c) Night 00-06 LT



d) Morning 06-12 LT

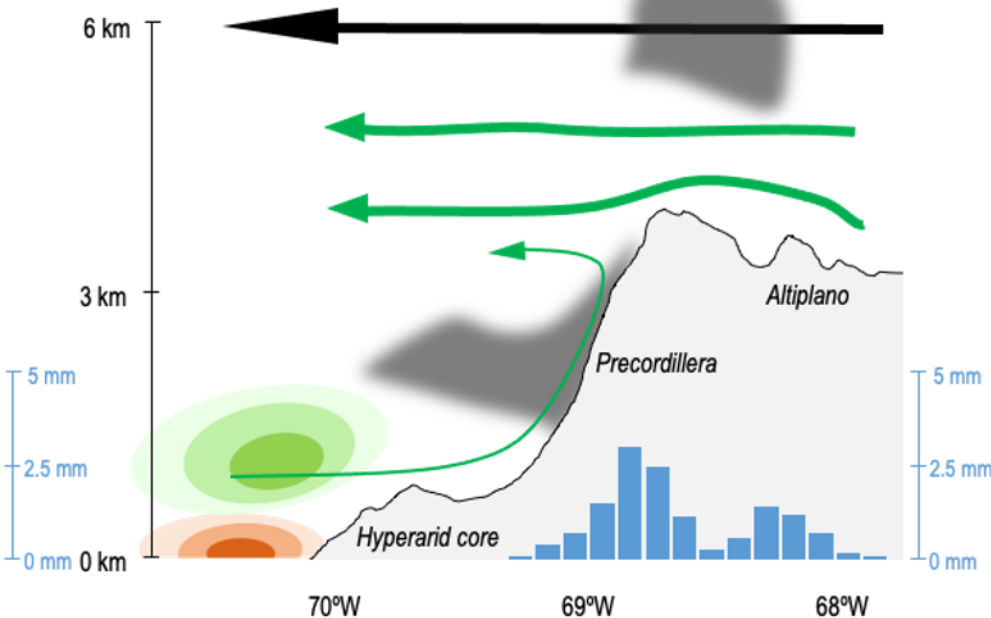
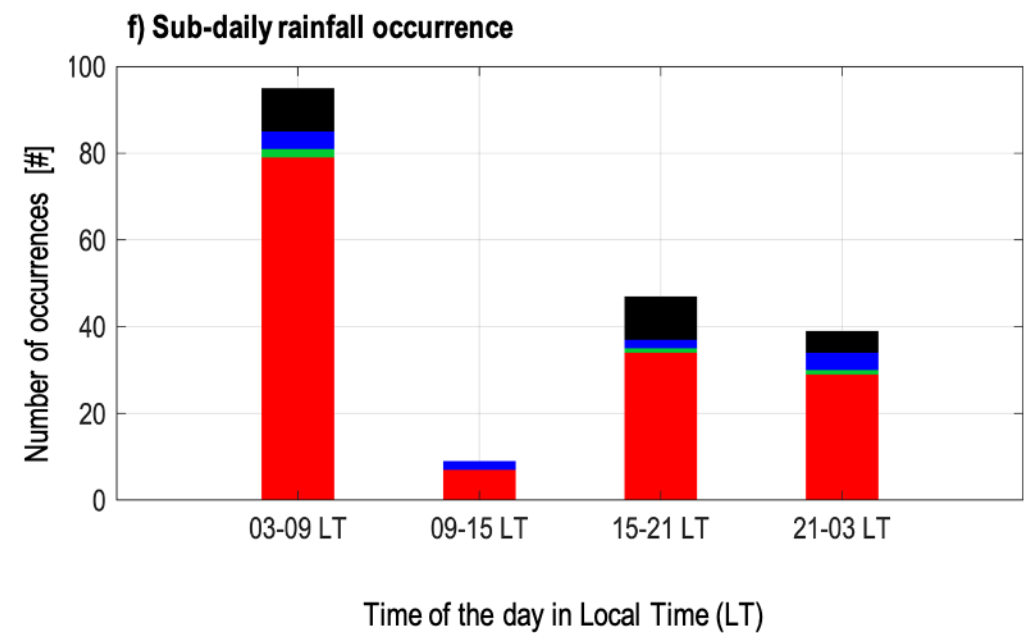
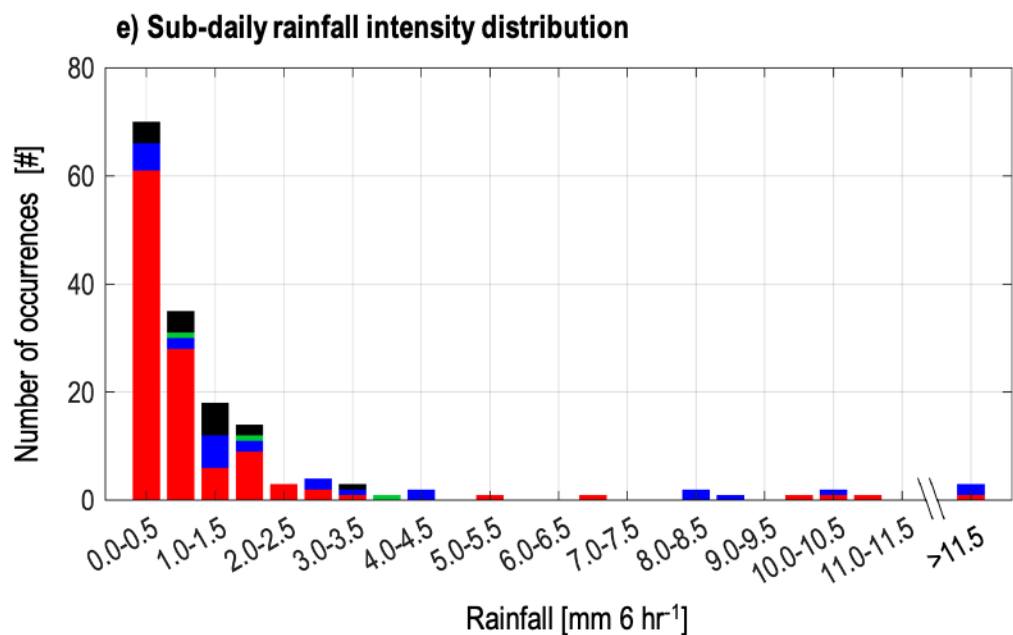
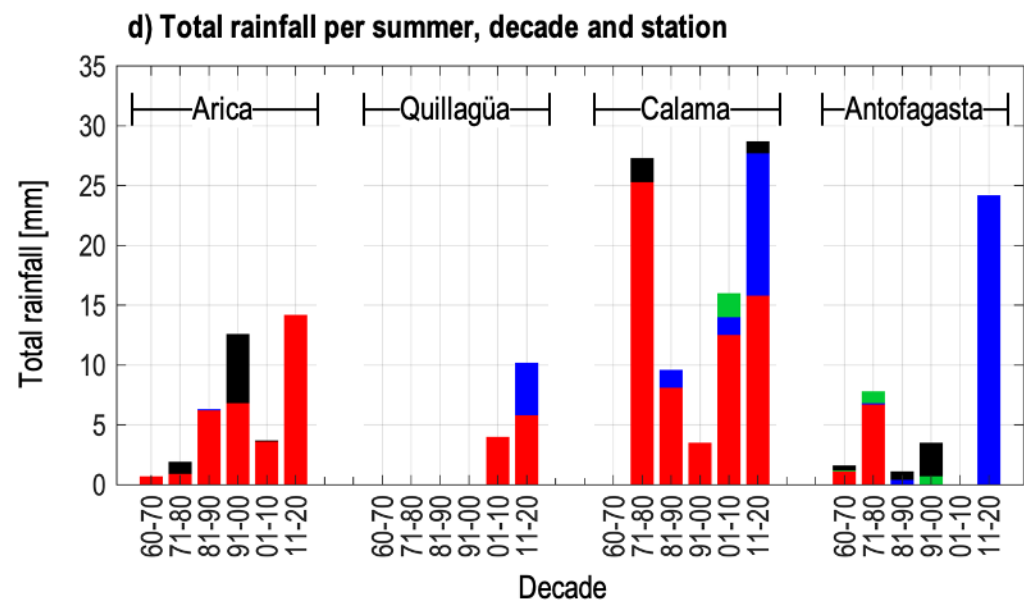
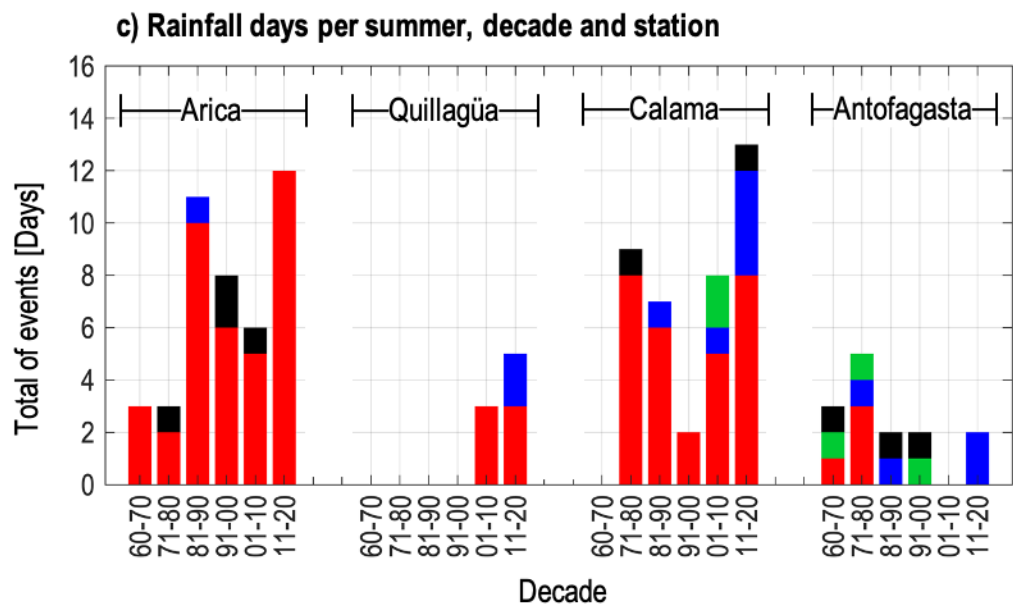
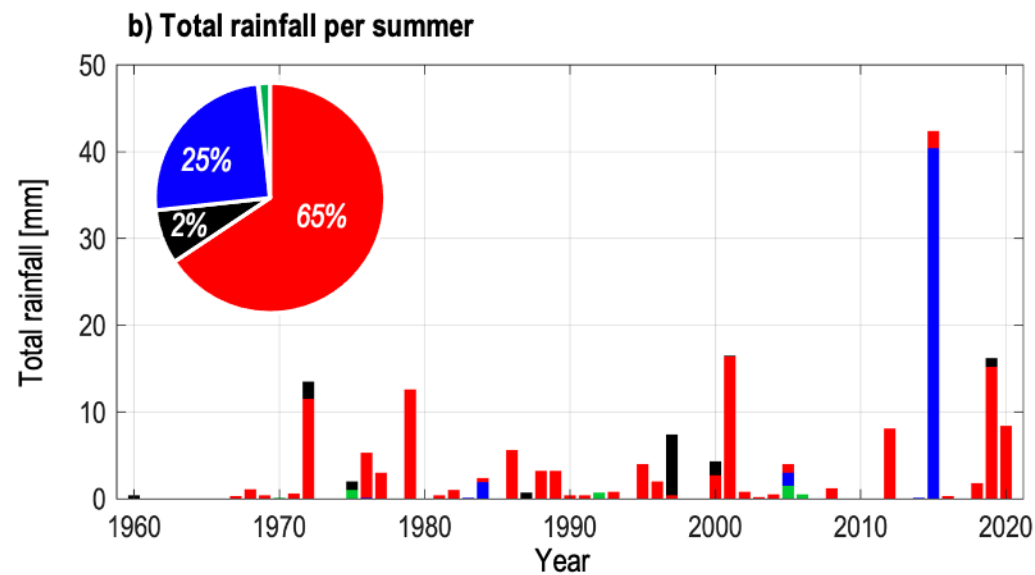
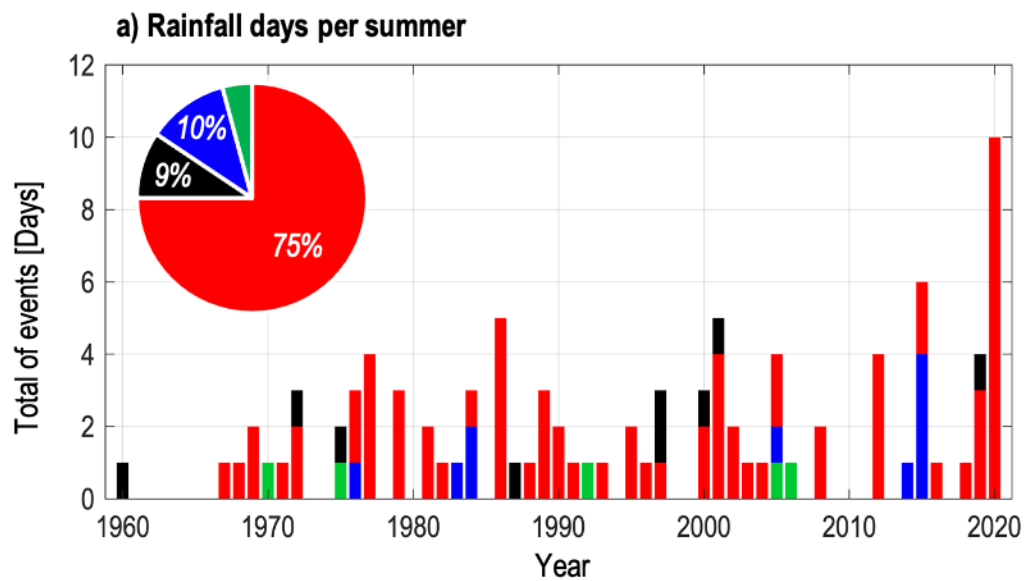


Figure 4.



■ Moist Northerlies (MN)
 ■ Bolivian High (BH)
 ■ Cut-off lows (COL)
 ■ Tropospheric troughs (TT)

Figure 5.

Figure 6.

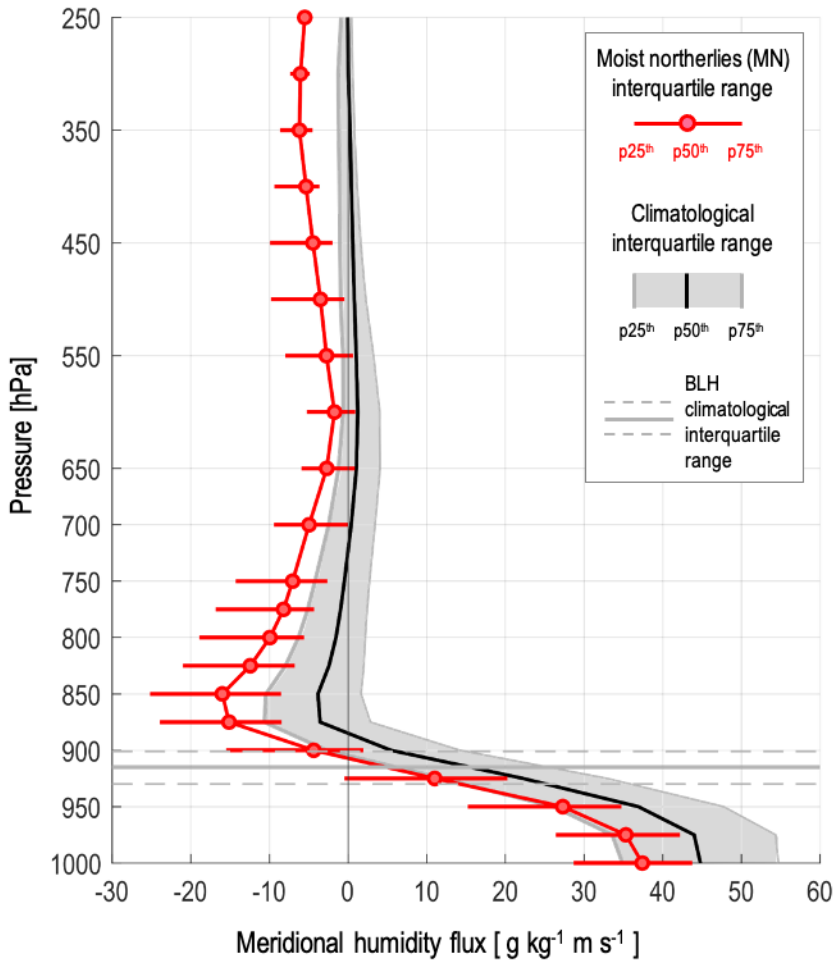
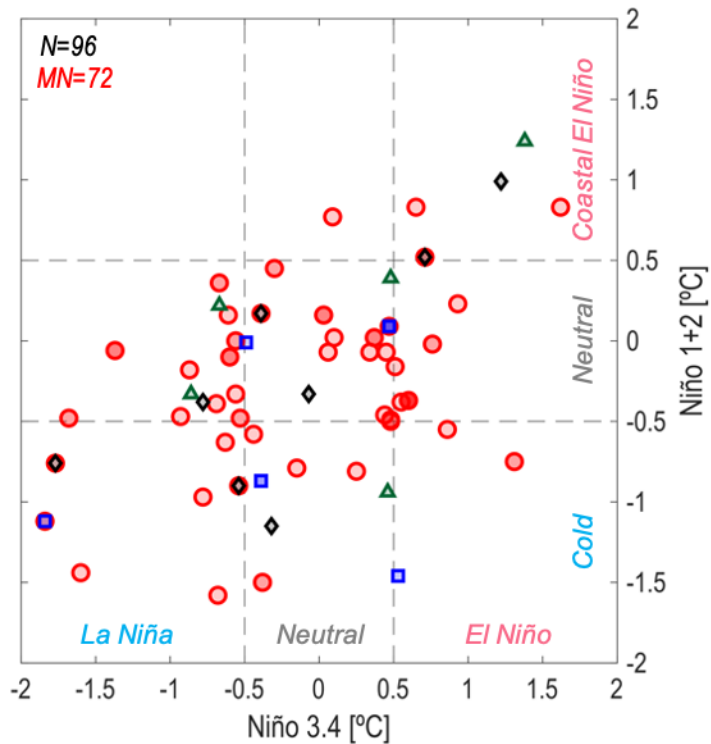
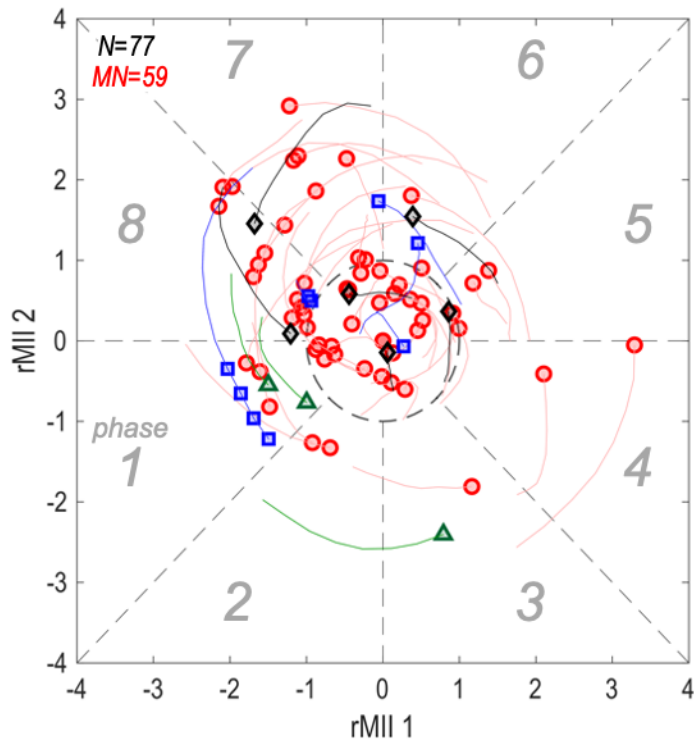


Figure 7.

a) Niño 3.4 and 1+2 index



b) MJO index



● Moist Northerlies (MN)
 ◆ Bolivian High (BH)
 ■ Cut-off lows (COL)
 ▲ Tropospheric troughs (TT)

Figure 8.

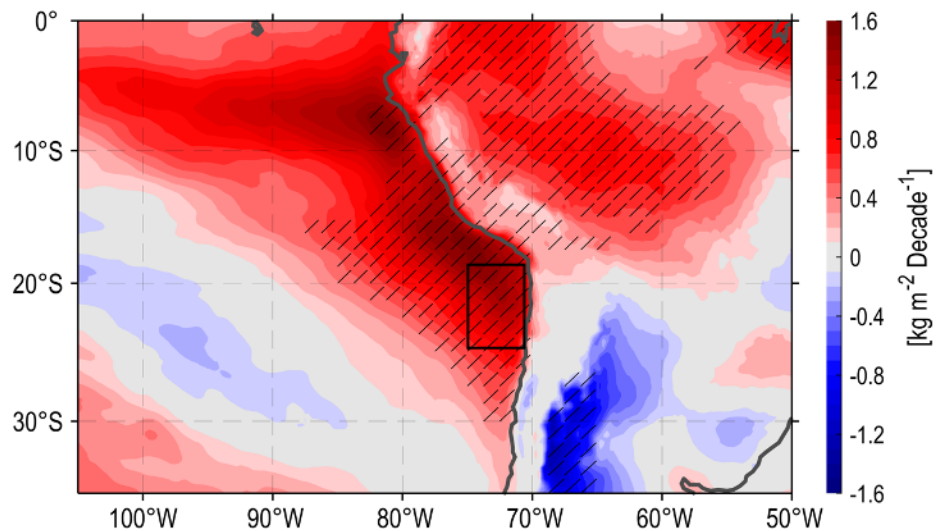
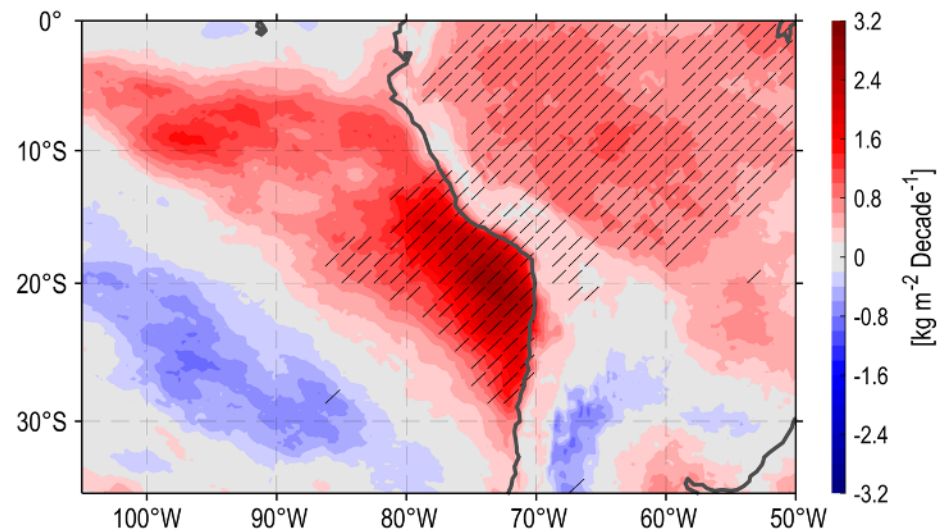
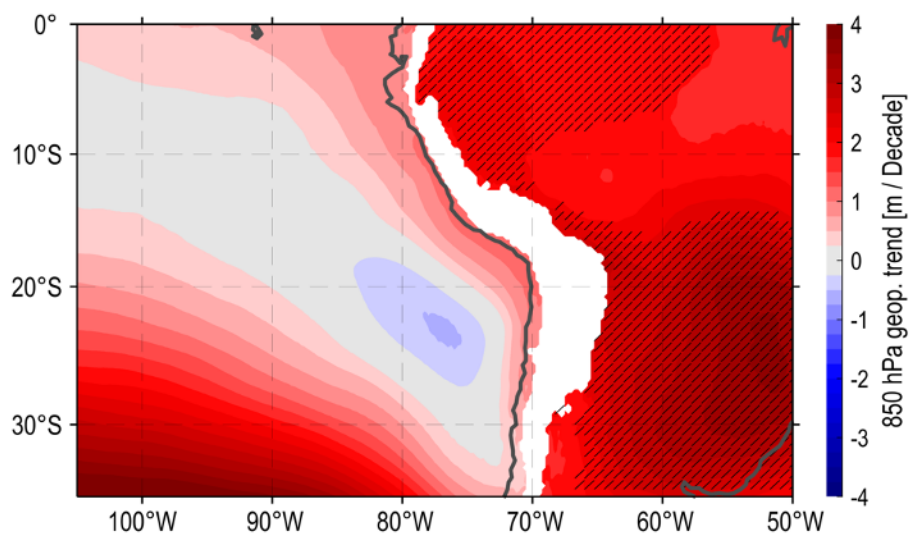
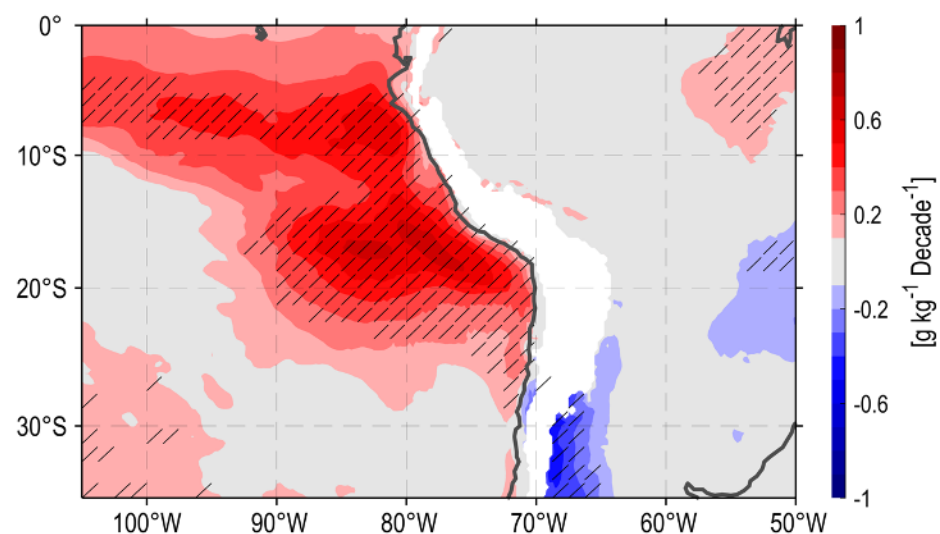
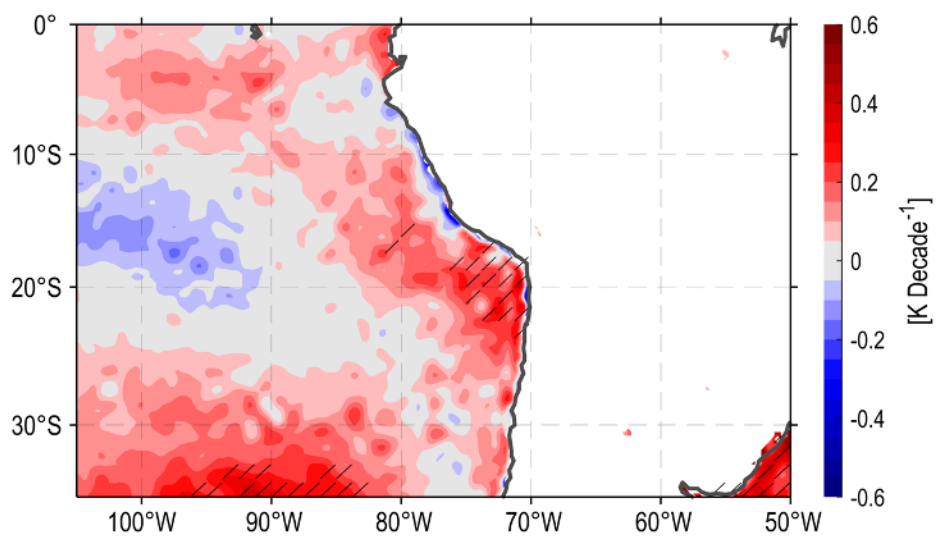
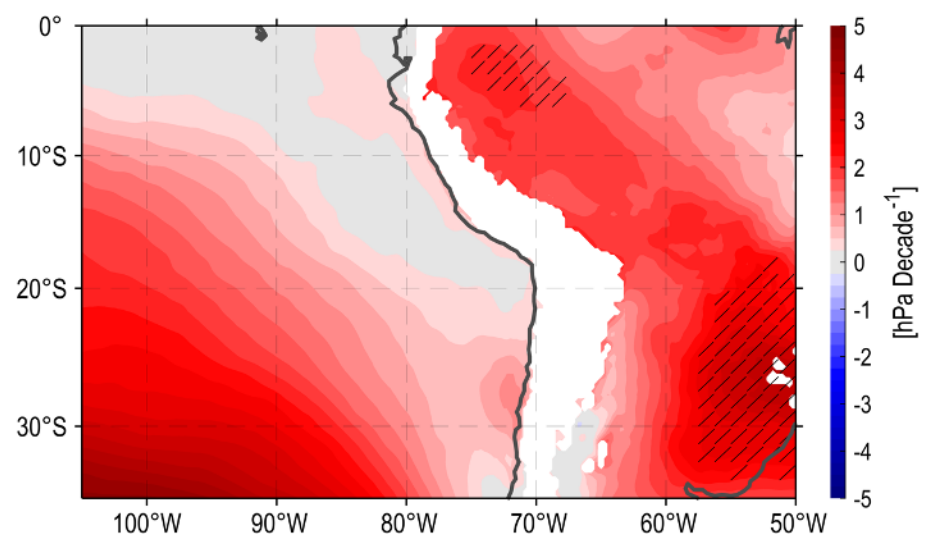
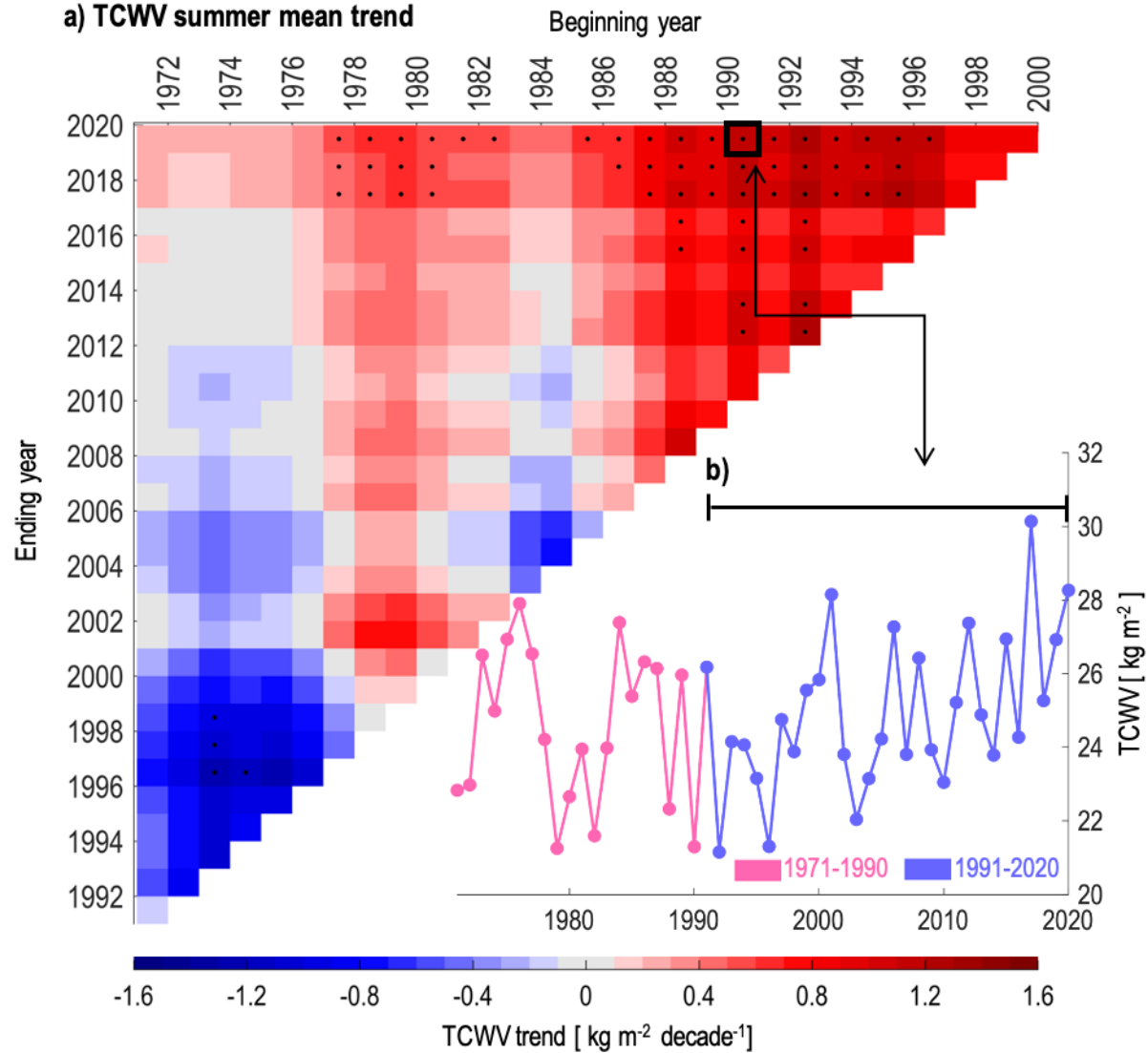
a) Mean summer TCWV**b) Summer TCWV 90th percentile****c) Summer mean 850 hPa geopotential height****d) Summer mean 850 hPa specific humidity****e) Summer mean sea surface temperature (SST)****f) Summer mean sea level pressure (SLP)**

Figure 9.

a) TCWV summer mean trend



c) TCWV daily mean probabilistic distribution

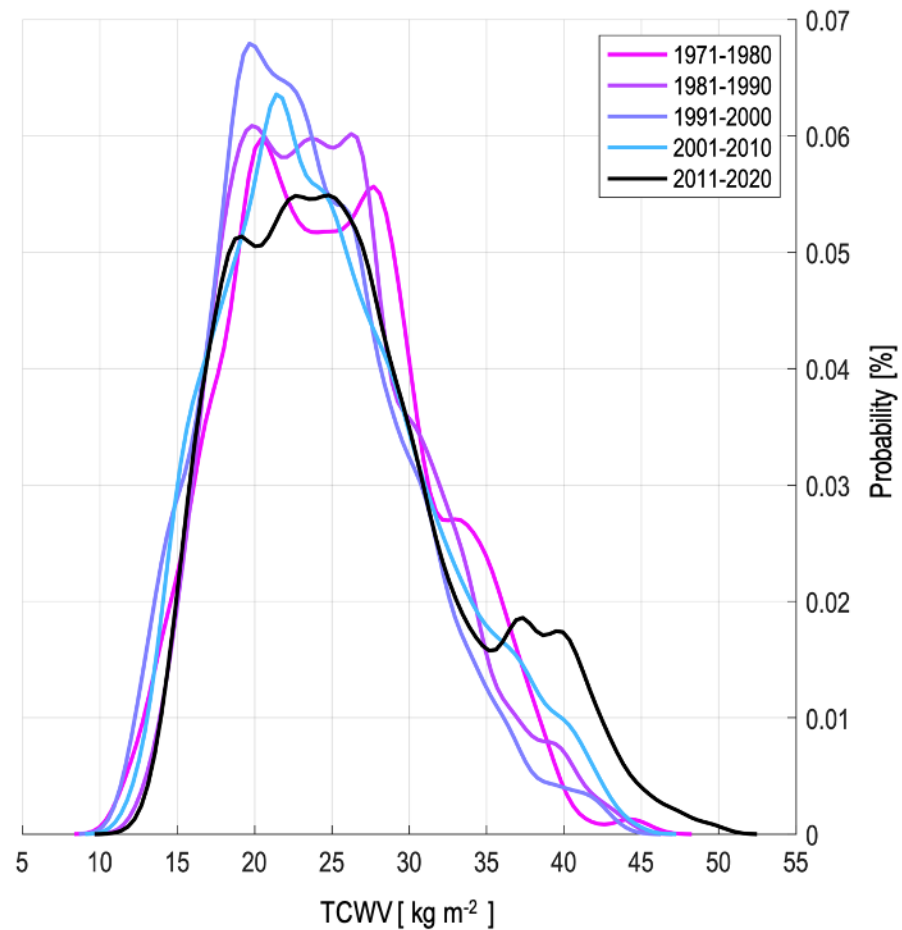


Figure 10.

a) Specific humidity trend**b) Meridional wind trend**